$D_s \to \eta, \eta'$ semileptonic decay form factors with disconnected quark loop contributions

Gunnar S. Bali,[1,2] Sara Collins,[1] Stephan Dürr,[3,4] and Issaku Kanamori[1,5,*]

[1]*Institute for Theoretical Physics, University of Regensburg, 93040 Regensburg, Germany*
[2]*Tata Institute of Fundamental Research, Homi Bhabha Road, Mumbai 400005, India*
[3]*Bergische Universität Wuppertal, Gaußstraße 20, 42119 Wuppertal, Germany*
[4]*Jülich Supercomputing Center, Forschungszentrum Jülich, 52425 Jülich, Germany*
[5]*Institute of Physics, National Chiao-Tung University, Hsinchu 30010, Taiwan*
(Received 3 July 2014; published 14 January 2015)

We calculate for the first time the form factors of the semileptonic decays of the D_s meson to η and η' using lattice techniques. As a by-product of the calculation we obtain the masses and leading distribution amplitudes of the η and η' mesons. We use $N_f = 2 + 1$ nonperturbatively improved clover fermions on configurations with a lattice spacing $a \sim 0.075$ fm. We are able to obtain clear signals for relevant matrix elements, using several noise reduction techniques, for both the connected and the disconnected contributions. This includes a new method for reducing the variance of pseudoscalar disconnected two-point functions. At zero momentum transfer, we obtain for the scalar form factors, $|f_0^{D_s \to \eta}| = 0.564(11)$ and $|f_0^{D_s \to \eta'}| = 0.437(18)$ at $M_\pi \approx 470$ MeV, as well as $|f_0^{D_s \to \eta}| = 0.542(13)$ and $|f_0^{D_s \to \eta'}| = 0.404(25)$ at $M_\pi \approx 370$ MeV, where the errors are statistical only.

PACS numbers: 12.38.Gc, 13.20.Fc, 14.40.Be, 14.40.Lb

I. INTRODUCTION

In general, semileptonic decays of charmed mesons are well studied both experimentally and theoretically, in particular, using lattice techniques. However, this is not the case for the D_s meson for which the main semileptonic modes are to the ϕ, η and η' mesons. Lattice studies of these decays are technically challenging due to the presence of disconnected quark-line contributions. So far only the form factor for the decay $D_s \to \phi \ell \bar{\nu}_\ell$ has been computed, omitting the disconnected contributions [1]. QCD sum rules provide an alternative approach based on the operator product expansion (OPE) and analyticity using the assumption of quark-hadron duality. There is one result using the standard local OPE in terms of condensates [2] and two using light cone OPE in terms of distribution amplitudes [3,4]. These studies utilize the η and η' distribution amplitudes, which, in principle, can be calculated on the lattice. A first principles calculation of the form factors for $D_s \to \eta^{(\prime)} \ell \bar{\nu}_\ell$ therefore can serve as a cross-check on the assumptions of the sum rule approach and is of phenomenological interest in itself, providing information on the internal structure of the mesons in the final state (see, for example, Ref. [5]). In terms of experimental results, there are no measurements of the form factors for these modes so far and only the branching fractions for $D_s \to \eta^{(\prime)} \ell \bar{\nu}_\ell$ have been determined by the CLEO Collaboration [6].

In this article, we report on our exploratory study of the D_s to $\eta^{(\prime)} \ell \bar{\nu}_\ell$ semileptonic decay form factors using lattice techniques. Some preliminary results have been presented in Refs. [7–9]. The relevant matrix elements for these decay modes are parametrized as follows:

$$\langle \eta^{(\prime)}(k) | V_\mu | D_s(p) \rangle = f_+(q^2) \left[(p+k)_\mu - \frac{M_{D_s}^2 - M_{\eta^{(\prime)}}^2}{q^2} q_\mu \right] + f_0(q^2) \frac{M_{D_s}^2 - M_{\eta^{(\prime)}}^2}{q^2} q_\mu, \tag{1}$$

where V_μ is a vector current at position[1] **0**, $q_\mu = p_\mu - k_\mu$ is the four-momentum transfer and M_{D_s} and $M_{\eta^{(\prime)}}$ are the masses of the D_s and the $\eta^{(\prime)}$ mesons, respectively. This matrix element is characterized by two form factors, $f_0(q^2)$ and $f_+(q^2)$. In this work we focus on the scalar form factor $f_0(q^2)$, which we can also obtain from a scalar current $S = \bar{s}c$ [10],

$$f_0(q^2) = \frac{m_c - m_s}{M_{D_s}^2 - M_{\eta^{(\prime)}}^2} \langle \eta^{(\prime)} | S | D_s \rangle. \tag{2}$$

We use this relation because the combination $(m_c - m_s)S$ [and therefore $f_0(q^2)$] is a renormalization group invariant, provided the vector mass difference $m_c - m_s = (\kappa_c^{-1} - \kappa_s^{-1})/(2a)$ is used. Equation (2) is also free of additive renormalization.

---

[1]In practice one averages $V_\mu(\mathbf{y}) e^{i\mathbf{q}\cdot\mathbf{y}}$ over all positions $\mathbf{y}$, injecting the spatial momentum $\mathbf{q}$ required by momentum conservation, to increase statistics.

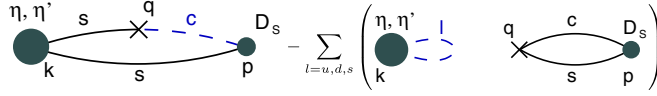*issaku.kanamori@physik.uni-regensburg.de

014503-1

FIG. 1 (color online). Connected (first term) and disconnected (second term) fermion loop diagrams. We use stochastic methods to calculate the blue dashed fermion lines. The labeling of the four-momenta p, q, k reflects the conventions adopted in Eq. (1).

The three-point function needed to compute the form factor contains quark-line disconnected loops (see Fig. 1). Often corrections from disconnected loops are numerically small. However, their impact on the three-point function is enhanced by a factor of about 3, due to the summation over three light quark flavors. Moreover, in the pseudoscalar case the disconnected quark loops couple to the axial anomaly. In spite of the computational expense and the inferior quality of the signal, relative to that of the quark-line connected contribution, the calculation of the disconnected contribution turns out to be feasible and its impact is significant [7,11]. Therefore, these decay modes also provide a perfect playground for testing a variety of techniques for calculating the disconnected quark-line loops.

We use QCDSF $N_f = 2 + 1$ configurations [12,13] that were generated using a novel approach for varying the sea quark masses, which is ideal for studying flavor physics in the SU(3) flavor basis. The flavor singlet mass average of the three light quarks, $\frac{1}{3}(m_u + m_d + m_s)$, is kept fixed so that the combination $2M_K^2 + M_\pi^2$ computed from the kaon mass, M_K, and pion mass, M_π, approximately coincides with the physical value. Starting from the flavor SU(3) symmetric point $(m_u = m_d = m_s)$, $m_l = m_u = m_d$ is reduced as m_s is increased.

The outline of this paper is as follows: in the next section we describe the technical details of the lattice calculation. Before we can address decays of the D_s meson into final states including the η or η' mesons, we have to construct the corresponding interpolators. Therefore, in Sec. III, we determine the mixing of the physical states relative to the octet-singlet basis. We present a new method to reduce statistical noise and obtain the η and η' masses and the leading distribution amplitudes. The details of the new method, described in Sec. III B, are quite technical and can be skipped by those readers who are primarily interested in the final results. In Sec. IV we describe our methods for extracting the matrix elements relevant for the computation of the form factors. Subsequently, these are obtained in the same section, before we conclude.

II. DETAILS OF THE LATTICE CALCULATION

The QCDSF $N_f = 2 + 1$ configurations were generated with the tree level Symanzik improved gluon action and the stout link nonperturbatively improved clover fermion action (SLiNC) [14]. We use the same action for the valence-only charm quark. The SLiNC action is on-shell

$O(a)$ improved. In general, there will be $O(a)$ correction term, $a\bar{s}\overleftrightarrow{D}_\mu\gamma_\mu c$, to Eq. (2). However, this term can be eliminated using the equations of motion, and one can show that the nonsinglet improvement coefficients $b_S = -2b_m$ [15,16] cancel from Eq. (2) so that $f_0(q^2)$ is automatically $O(a)$ improved.

The parameters are summarized in Table I. So far we have used only one lattice spacing $a \sim 0.075$ fm (determined using the quantity w_0 proposed in Ref. [17]), and one volume $V_4 = L^3 T = 24^3 \times 48a^4$, which corresponds to a physical spatial extent $L \sim 1.8$ fm. Our value of the lattice spacing is about 10% smaller than the value of Refs. [12,13] ($a \sim 0.083$ fm) which was obtained from the average octet baryon mass, but is consistent with a newer determination ($a \sim 0.074(2)$ fm) in Ref. [18]. We analyzed 939 configurations at the flavor symmetric point $(m_l = m_s)$, for which $M_\pi = M_K = 470.5(1.8)$ MeV (Set S), and 239 configurations $(m_l < m_s)$ with $M_\pi = 370.1(3.3)$ MeV and $M_K = 509.1(2.7)$ MeV (Set A). Because of the different value for the lattice spacing, these masses differ from the numbers given in Refs. [12,13]. In particular, the average octet pion mass exceeds the experimental value $[(M_\pi^2 + 2M_K^2)/3]^{1/2} \approx 411$ MeV by about 60 MeV, meaning that extrapolating to the physical pion mass, we would end up with unphysically heavy kaons. The charm quark mass m_c was tuned so that the spin averaged 1S charmonium mass, $M_{\overline{1S}} = \frac{1}{4}(M_{\eta_c} + 3M_{J/\psi})$, corresponds to the experimental value [19].

In order to reduce autocorrelations, the configurations were sampled every 5 Monte Carlo trajectories for Set S and every 10 trajectories for Set A. In addition, the location of the source was chosen randomly on each configuration. However, significant correlations were found in the data when calculating the masses of the π, η and η' mesons, and we chose a conservative bin size of 5 (25 molecular dynamics time units) for Set S and 2 (20 molecular dynamics time units) for Set A. The mass of the D_s, the mixing angle discussed in Sec. III C and the form factor, $f_0(q^2)$, did not show any significant autocorrelations, so we did not use binning for these observables.

For all source and sink interpolators, we used a gauge invariant Gaussian smearing (Wuppertal smearing [20,21]) with APE smeared gauge fields [22] in the spatial directions.

TABLE I. The simulation parameters. Set S corresponds to the SU(3) flavor symmetric point where the pion, kaon, and eta mesons are mass-degenerate while in Set A the symmetry between the strange quark and the light quarks is broken. The lattice size is $24^3 \times 48$ in both cases and $\beta = 10/g^2$, rather than $\beta = 6/g^2$.

Set	β	κ_l	κ_s	M_π	LM_π	Configurations
S	5.5	0.12090	0.12090	470.5(1.8) MeV	4.3	939
A	5.5	0.12104	0.12062	370.1(3.3) MeV	3.3	239

The smearing parameters were chosen to minimize excited state contributions to the connected two-point functions.

Disconnected fermion loops appear in both two- and three-point functions. These loops need to be evaluated at different times and momenta. They can be obtained from the inverse of the dimensionless lattice Dirac operator, M, in the following way:

$$C_{1\,\text{pt}}(t, \boldsymbol{p}; x_0) = \sum_{\boldsymbol{x}} \exp(i\boldsymbol{p} \cdot (\boldsymbol{x} - x_0)) \text{tr}$$
$$\times \left[\sum_{\boldsymbol{x}', \boldsymbol{x}''} \Gamma \phi(\boldsymbol{x}, \boldsymbol{x}'') M^{-1}(t, \boldsymbol{x}''; t, \boldsymbol{x}') \phi(\boldsymbol{x}', \boldsymbol{x}) \right],$$
(3)

where the Dirac matrix for a pseudoscalar meson is $\Gamma = \gamma_5$ and ϕ is the smearing function. The origin for the Fourier transformation is denoted as x_0. Since M satisfies γ_5 Hermiticity, the smearing function is Hermitian and commutes with γ_5, the disconnected loop is real in coordinate space and $C_{1\,\text{pt}}(t, \boldsymbol{p}) = C_{1\,\text{pt}}(t, -\boldsymbol{p})^*$. Details of the estimation of the disconnected loops are given in Appendix A.

III. η AND η' STATES

Prior to determining decays of the D_s into the η or η' mesons, we have to construct these physical states. We first discuss the general mixing formalism, relative to the octet-singlet basis, then determine the respective masses and compare our results to other studies. In Sec. III B, which is technical and can be skipped on first reading, we discuss a particular problem we encountered, due to the insufficient sampling across topological sectors on one of our ensembles. The method we suggest to resolve this turns out to be of a more general applicability and significantly reduces statistical errors. Finally, in Sec. III C we determine mixing angles and leading distribution amplitudes of these states.

A. Extracting physical states

The correct creation operators for the η and η' states are *a priori* unknown in the flavor nonsymmetric case (Set A). We start from singlet $\eta_1 = \frac{1}{\sqrt{3}}(u\bar{u} + d\bar{d} + s\bar{s})$ and octet $\eta_8 = \frac{1}{\sqrt{6}}(u\bar{u} + d\bar{d} - 2s\bar{s})$ states and first calculate a 2×2 correlation matrix of two-point functions[2]

$$\langle C_{2\,\text{pt}}(t, \boldsymbol{p}) \rangle = \begin{pmatrix} \langle C_{2\,\text{pt}}^{88}(t, \boldsymbol{p}) \rangle & \langle C_{2\,\text{pt}}^{81}(t, \boldsymbol{p}) \rangle \\ \langle C_{2\,\text{pt}}^{18}(t, \boldsymbol{p}) \rangle & \langle C_{2\,\text{pt}}^{11}(t, \boldsymbol{p}) \rangle \end{pmatrix}$$
$$\equiv \begin{pmatrix} \langle \mathcal{O}_8(t; \boldsymbol{p}) \mathcal{O}_8^\dagger(0) \rangle & \langle \mathcal{O}_8(t; \boldsymbol{p}) \mathcal{O}_1^\dagger(0) \rangle \\ \langle \mathcal{O}_1(t; \boldsymbol{p}) \mathcal{O}_8^\dagger(0) \rangle & \langle \mathcal{O}_1(t; \boldsymbol{p}) \mathcal{O}_1^\dagger(0) \rangle \end{pmatrix},$$
(4)

---

[2]We always use $\langle \cdot \rangle$ for expectation values so that the correlation functions without $\langle \cdot \rangle$ like $C_{1\,\text{pt}}(\boldsymbol{p}, t)$ and $C_{2\,\text{pt}}(\boldsymbol{p}, t)$ denote configuration by configuration quantities.

where $\mathcal{O}_8$ and $\mathcal{O}_1$ are smeared interpolators for the octet and singlet states, respectively. Each element includes disconnected fermion loop contributions. The latter were averaged over all possible source positions x_0 in space and time, shifting the source and the sink accordingly. For the connected part, we used low mode averaging [23,24]. We describe the details of these calculations in Appendix B. We solve the following generalized eigenvalue problem:

$$\langle C_{2\,\text{pt}}(t_0, \boldsymbol{p}) \rangle^{-\frac{1}{2}} \langle C_{2\,\text{pt}}(t, \boldsymbol{p}) \rangle v_\alpha(t, \boldsymbol{p})$$
$$= \lambda_\alpha(t, \boldsymbol{p}) \langle C_{2\,\text{pt}}(t_0, \boldsymbol{p}) \rangle^{\frac{1}{2}} v_\alpha(t, \boldsymbol{p}),$$
(5)

where $\lambda_\alpha(t, \boldsymbol{p})$ ($\alpha = \eta, \eta'$) is the generalized eigenvalue and $v_\alpha(t, \boldsymbol{p})$ is the generalized eigenvector. The time slice t_0 can be varied to minimize the excited state contributions to λ_α and v_α. We tried $t_0/a = 1$–3 and found no significant difference in the results, so we use $t_0/a = 1$ which gives the largest range of $t > t_0$. We parametrize the eigenvectors of the two-dimensional system in the following way:

$$v_\eta(t, \boldsymbol{p}) = (\cos\theta(t, \boldsymbol{p}), -\sin\theta(t, \boldsymbol{p}))^T,$$
$$v_{\eta'}(t, \boldsymbol{p}) = (\sin\theta'(t, \boldsymbol{p}), \cos\theta'(t, \boldsymbol{p}))^T.$$
(6)

Note that in general $\theta \neq \theta'$. In the large t limit, the ground state dominates, $v_{\eta^{(\prime)}}(t, \boldsymbol{p}) \to v_{\eta^{(\prime)}}(\boldsymbol{p})$ and we can obtain the interpolators for the physical ground states,

$$\mathcal{O}_\eta = \cos\theta(\boldsymbol{p})\mathcal{O}_8 - \sin\theta(\boldsymbol{p})\mathcal{O}_1,$$
$$\mathcal{O}_{\eta'} = \sin\theta'(\boldsymbol{p})\mathcal{O}_8 + \cos\theta'(\boldsymbol{p})\mathcal{O}_1.$$
(7)

It is sufficient to extract $\sin\theta$ and $\sin\theta'$. This was done by fitting the corresponding components of $v_\alpha(t, \boldsymbol{p})$ to a constant, taking into account correlations including those between $\sin\theta$ and $\sin\theta'$ and those between different time slices. Using Eq. (7), we can construct the two-point functions of the physical states for each $\boldsymbol{p}$,

$$\langle C_{2\,\text{pt}}^\eta(t, \boldsymbol{p}) \rangle = \langle \mathcal{O}_\eta(t; \boldsymbol{p}) \mathcal{O}_\eta(0) \rangle,$$
$$\langle C_{2\,\text{pt}}^{\eta'}(t, \boldsymbol{p}) \rangle = \langle \mathcal{O}_{\eta'}(t; \boldsymbol{p}) \mathcal{O}_{\eta'}(0) \rangle.$$
(8)

The energy of the state α at a momentum $\boldsymbol{p}$, $E_\alpha(\boldsymbol{p})$, can then be obtained by fitting these two-point functions at sufficiently large times t to the functional form

$$\langle C_{2\,\text{pt}}^\alpha(t, \boldsymbol{p}) \rangle = A_\alpha(\boldsymbol{p})(\exp[-tE_\alpha(\boldsymbol{p})]$$
$$+ \exp[-(T - t)E_\alpha(\boldsymbol{p})]),$$
(9)

where T is the temporal lattice extent, and $A_\alpha(\boldsymbol{p})$ is a (momentum-dependent) amplitude.

At zero momentum the situation is more involved and we deviate from the above procedure; see Sec. III B. For the η' mass on Set A and Set S and the η mass on Set A, the statistical error of $M_\alpha = E_\alpha(\boldsymbol{0})$ could be further reduced by
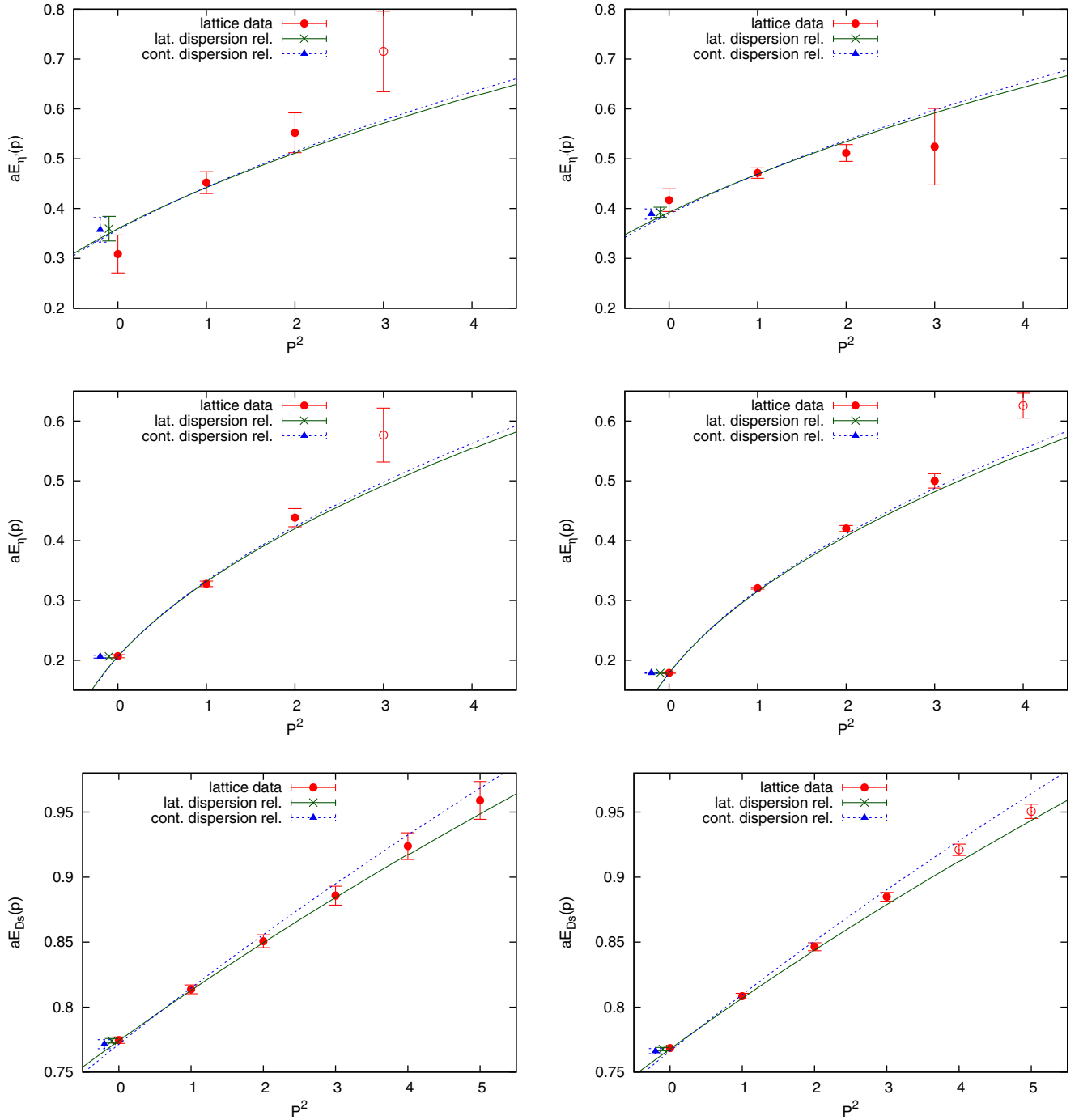
FIG. 2 (color online).   Energies $E(\boldsymbol{p})$ along with fitted lattice and continuum dispersion relations of the η' (top), η (middle) and D_s (bottom) mesons at $M_\pi \approx 370$ MeV (Set A, left) and at the SU(3) flavor symmetric point $M_\pi \approx 470$ MeV (Set S, right). The momentum $\boldsymbol{P} = \boldsymbol{p} \times L/(2\pi)$ is in lattice units. Open circles were excluded from the fits. $E(\boldsymbol{p} = \boldsymbol{0})$ for η (Set A) and η' (Sets A, S) were obtained by using the improved method explained in Sec. III B. For clarity, the different mass determinations are replotted at $\boldsymbol{P}^2 = 0$ with a slight horizontal shift.

fitting zero- and nonzero-momentum data to the lattice dispersion relation

$$2\cosh(aE(\boldsymbol{p})) = 2\cosh(aM) + \sum_{i=1}^{3} 4\sin^2\frac{ap_i}{2}, \quad (10)$$

where the mass, aM, is a free parameter. This is illustrated in Fig. 2, where the energies we obtained directly at zero and at finite momenta, and the fitted dispersion relations and their results are shown. The masses are listed in Table II, and the energies at zero and finite momenta in Tables VII and VIII of Appendix D. The η meson at the

TABLE II.   Masses of the η and the η' mesons. The errors are statistical only.

Set	M_η [MeV]	$M_{\eta'}$ [MeV]
S	470.5 (1.8)	1032 (27)
A	542.8 (6.2)	946 (65)

SU(3) flavor symmetric point (Set S) is identical to the pion (and the kaon) and the precision of its mass did not benefit from including nonzero momentum data. In this case we display the $\boldsymbol{p} = \boldsymbol{0}$ result in the table. No significant differences were found for the η and η' masses if the continuum dispersion relation $E^2 = M^2 + \boldsymbol{p}^2$ was used instead, as seen in the figure. For comparison, we also show the D_s data in the figure. For this meson, the lattice dispersion relation is clearly preferred by the data: the χ^2 values, normalized with respect to the degrees of freedom, $\chi^2/\text{d.o.f.}$, were poor (4.7 for Set S and 2.2 for Set A) and did not reproduce the data. In Fig. 2, uncorrelated fits are shown in these cases.

In Fig. 3, we plot the effective masses of the η, the η' and the π. The fitted η and η' masses, with the exception of the $\eta = \eta_8 = \pi$ at the SU(3) symmetric point, were obtained using the improved method detailed in the next subsection. The masses are $M_\eta = 470.5(1.8)$ MeV and $M_{\eta'} = 1032(27)$ MeV for Set S ($M_\pi \approx 470$ MeV), $M_\eta = 542.8(6.2)$ MeV and $M_{\eta'} = 946(65)$ MeV for Set A ($M_\pi \approx 370$ MeV), where the errors are statistical only. These values are consistent with the finite momentum data shown in Fig. 2.

In Fig. 4 we compare our η and η' masses to results obtained by other lattice collaborations [25–28] and the respective experimental values [29]. In some of these studies the extrapolation to the physical point was performed, however, for consistency we do not show extrapolated values. Note that, since the flavor singlet quark mass average is kept fixed in our simulations, the mass of the η approaches the physical point from below. Our results seem

to approach the experimental values, and the η' masses are consistent with other lattice determinations that were obtained keeping the strange quark mass approximately constant.

B. Finite volume effects on the η and η' masses

Analyzing Set S we found that the $\eta'(= \eta_1)$ two-point function at large times t does not decay to zero [cf. Eq. (9)] but instead saturates at a small nonzero value. This phenomenon can be explained as a finite volume effect, coupled to unrealistic fluctuations of the topological charge, due to an insufficient sampling of the topological sectors within our limited statistics. We will see that this can be cured by defining an improved observable which also reduces the variance of disconnected pseudoscalar two-point functions in the case of a correctly sampled topological charge.

The disconnected contributions can be obtained by correlating pairs of momentum-projected "1-point loops." The sum over such a one-point loop is proportional to the fermionic definition of the topological charge Q_f,

$$\sum_t C_{1\,\text{pt}}(t, \boldsymbol{p} = \boldsymbol{0}) = \sum_t \sum_{\boldsymbol{x}} C_{1\,\text{pt}}(t, \boldsymbol{x}) = \alpha Q_f \approx \alpha Q,$$

(11)

where the (dimensionless) proportionality constant α will depend on the quark mass, the smearing function and the normalization of the interpolator, and we assume the fermionic and gluonic definitions of the topological charge to agree $Q \approx Q_f$. The above relation suggests an approximate proportionality between the topological charge density and the fermionic one-point loop: $\rho(t, \boldsymbol{x}) \simeq C_{1\,\text{pt}}(t, \boldsymbol{x})/(\alpha a^4)$.

If the topological charge is fixed to Q, point-point correlators of the topological charge density $\rho(x)$ will remain finite for large separations $|x|$ [30],
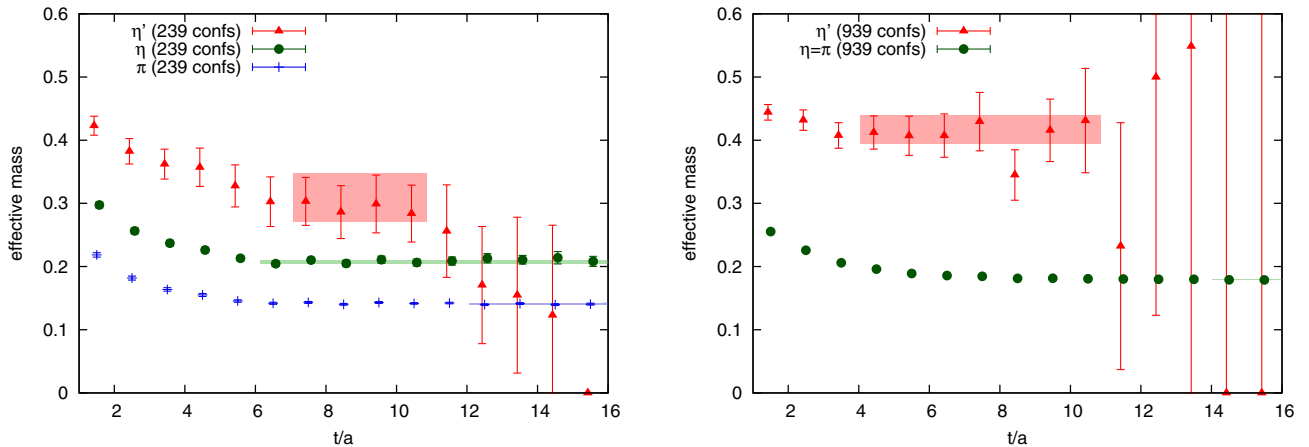

FIG. 3 (color online).   Effective masses of the π, η and η' for (left) $M_\pi \approx 370$ MeV (Set A) and (right) $M_\pi \approx 470$ MeV (Set S). Note that for Set S $\pi = \eta = \eta_8$ and $\eta' = \eta_1$.

$$\langle \rho(x)\rho(0)\rangle_Q \to \frac{1}{V_4}\left(\frac{Q^2}{V_4} - \chi_t - \frac{c_4}{2\chi_t V_4}\right) + \cdots, \quad (12)$$

where V_4 is the physical four-volume, χ_t is the topological susceptibility, and the dimensionful kurtosis c_4 parametrizes the leading deviations from Gaussian fluctuations of Q.

Projecting the above expression onto a fixed spatial momentum, the constant term only affects the $\boldsymbol{p} = \boldsymbol{0}$ case.

Using $\rho(x) \simeq C_{1\,\mathrm{pt}}(x)/(\alpha a^4)$, we obtain the following estimate of the η' two-point function, which is the singlet two-point function [see Eq. (B2)] in the SU(3) flavor symmetric case:

$$C_{2\,\mathrm{pt}}^{\eta'}(t,\boldsymbol{p}=\boldsymbol{0}) = C_{\mathrm{conn}}(t,\boldsymbol{p}=\boldsymbol{0}) - 3\frac{a^4}{V_4}\sum_{t_0/a=0}^{T/a-1} C_{1\,\mathrm{pt}}(t+t_0,\boldsymbol{p}=\boldsymbol{0})C_{1\,\mathrm{pt}}(t_0,\boldsymbol{p}=\boldsymbol{0})$$

$$= C_{\mathrm{conn}}(t,\boldsymbol{p}=\boldsymbol{0}) - 3\frac{\alpha^2 a^{12}}{V_4}\sum_{t_0/a=0}^{T/a-1}\sum_{\boldsymbol{x},\boldsymbol{x_0}} \rho(t+t_0,\boldsymbol{x})\rho(t_0,\boldsymbol{x_0}). \quad (13)$$

Here C_{conn} is the quark-line connected part of the two-point function and T is the temporal extent of the lattice. By using Eq. (12) and the observation that c_4 is negligible for our ensembles, we obtain

$$\langle C_{2\,\mathrm{pt}}^{\eta'}(t,\boldsymbol{p}=\boldsymbol{0})\rangle_Q \to \frac{3\alpha^2 a^5}{T}\left(\chi_t - \frac{Q^2}{V_4}\right) \quad (14)$$

for large t, resulting in the prediction for the finite volume effect at $|Q| = 0$,

$$\langle C_{2\,\mathrm{pt}}^{\eta'}(t,\boldsymbol{p}=\boldsymbol{0})\rangle_{Q=0} \to \frac{3\alpha^2 a^5 \chi_t}{T} \quad (m_l = m_s). \quad (15)$$

For the non-SU(3) flavor symmetric case, in principle, both the singlet and the octet parts of the η' two-point function should contribute to the constant. However, using only the singlet part gives a good approximation because $\sin\theta'$ in

Eq. (7) is small. The singlet-to-singlet contribution to the η' two-point function is

$$\langle C_{2\,\mathrm{pt}}^{\eta'}(t,\boldsymbol{p})\rangle = \cos^2\theta'\langle \mathcal{O}_1(t,\boldsymbol{p})\mathcal{O}_1^\dagger(0)\rangle + \cdots, \quad (16)$$

and we obtain

$$\langle C_{2\,\mathrm{pt}}^{\eta'}(t,\boldsymbol{p}=\boldsymbol{0})\rangle_{Q=0} \to \cos^2\theta'\frac{3\alpha^2 a^5 \chi_t}{T} \quad (m_l \neq m_s), \quad (17)$$

where we used a flavor-averaged proportionality constant[3]

$$\sum_t \frac{1}{3}[2C_{1\,\mathrm{pt}}^l(t,\boldsymbol{p}=\boldsymbol{0}) + C_{1\,\mathrm{pt}}^s(t,\boldsymbol{p}=\boldsymbol{0})] = \alpha Q. \quad (18)$$

To check Eq. (14), we measured Q using an improved field strength tensor [31] on smeared gauge fields with 90 iterations of Stout [32] smearing. The measured values clustered around integer values as expected. For each integer $n \geq 0$, using configurations with $n - 0.5 \leq |Q| < n + 0.5$ only (we denote them as $|Q| = n$ configurations), we calculated the two-point function of the η' at zero momentum. The values of the two-point functions in the large time limit exhibit a clear dependence on $|Q|$; see Fig. 5. Moreover, the constants obtained by fitting within such subsets are consistent with the linear dependence on Q^2 suggested by Eq. (14); see Fig. 6. See Ref. [33] for an earlier observation of the $|Q|$ dependence of the η' effective mass, Ref. [34] for the general argument and Ref. [35] for a fixed topology approach.

In Fig. 6, we also plot the $Q = 0$ predictions. These were obtained from Eq. (15) (Set S) and Eq. (17) (Set A). The topological susceptibilities $\chi_t = \langle Q^2\rangle/V_4$ were computed using the gluonic definition of the topological charge and

FIG. 4 (color online).   Summary plot of recent lattice determinations of the η (open symbols) and η' (solid symbols) masses. Results are shown from the RBC/UKQCD (2010, [25]), UKQCD (2011, [26]), HSC (2011, [27]), and ETMC (2013, [28]) Collaborations. The experimental values are taken from the Particle Data Group [29].

---

[3]For each flavor $a = l, s$, we have $\sum_t C_{1\,\mathrm{pt}}^a(t,\boldsymbol{p}=\boldsymbol{0}) = \alpha_a Q$, where the proportionality constant depends on the flavor through the quark mass. α in Eq. (18) can be written as $\alpha = (2\alpha_l + \alpha_s)/3$.
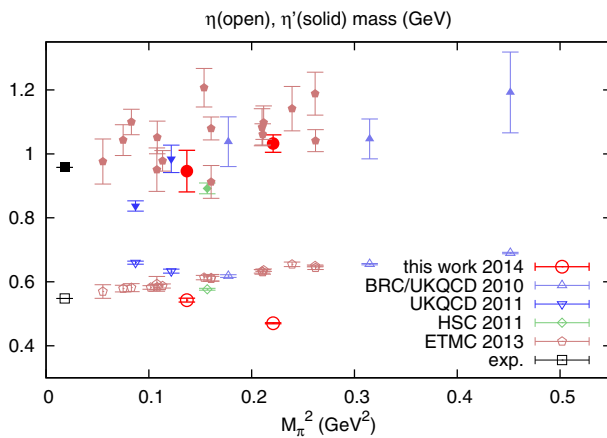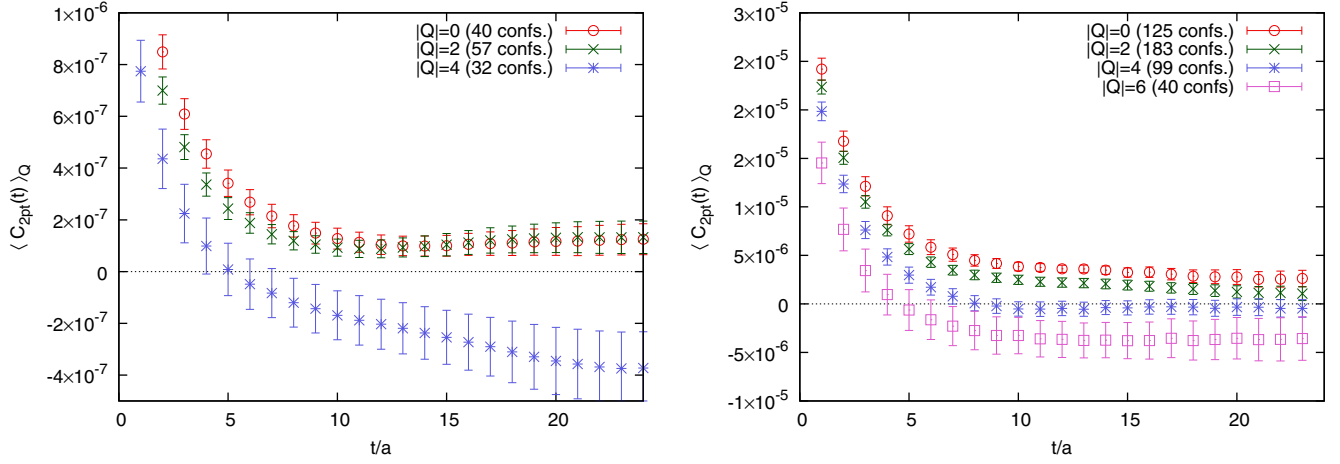
FIG. 5 (color online). The naive zero-momentum η' two-point function for each topological sector, for Set A (left panel) and Set S (right panel).

the parameters α were obtained by fitting the one-point loops as a function of the gluonic topological charge Q as in Eq. (18). For Set A we find consistency between the linear extrapolation and this $Q = 0$ prediction. On Set S, however, the prediction is significantly smaller than the extrapolated value, and also smaller than the measured values. At the same time the η' two-point function, averaged over all configurations, approaches a nonzero (positive) value. The linear fit of the constant part versus Q^2 crosses zero at a value $\langle Q^2 \rangle \approx 13$. Replacing the measured value $\chi_t = \langle Q^2 \rangle / V_4 = 9.1(0.4)/V_4$ within Eq. (15) by $13/V_4$, the prediction would be compatible with the fixed topology measurements. These observations are coherent with our above arguments and strongly suggest $\langle Q^2 \rangle$ on Set S to be underestimated, due to an insufficient sampling.

While the distribution of Q on Set S is too narrow, we find $\langle Q \rangle = 0$ within errors on both ensembles. Therefore, replacing $C_{1\,\mathrm{pt}} \mapsto C_{1\,\mathrm{pt}} - \langle C_{1\,\mathrm{pt}} \rangle$ within the above two-point

functions will not affect any expectation value or correct for the sampling of topological sectors in Set S. Nevertheless, we checked whether this procedure reduced the statistical noise, but we did not find any improvement.

One way of addressing the problem of a nonvanishing expectation value of the two-point function at large Euclidean times is simply to fit the correlation function to a constant plus an exponential decay (which we denote as "naive fit with a constant"). We adopted, however, a different strategy that we found to reduce the gauge noise: this is motivated by the results in Fig. 6, which suggest that the two-point functions are shifted by different values in different topological sectors according to Eq. (14). Therefore, normalizing the result to the $Q = 0$ sector may reduce the gauge fluctuations. We first add a term that cancels the Q^2 dependence of Eq. (12), and then fit the result to a constant plus an exponential decay (denoted as the "improved method").
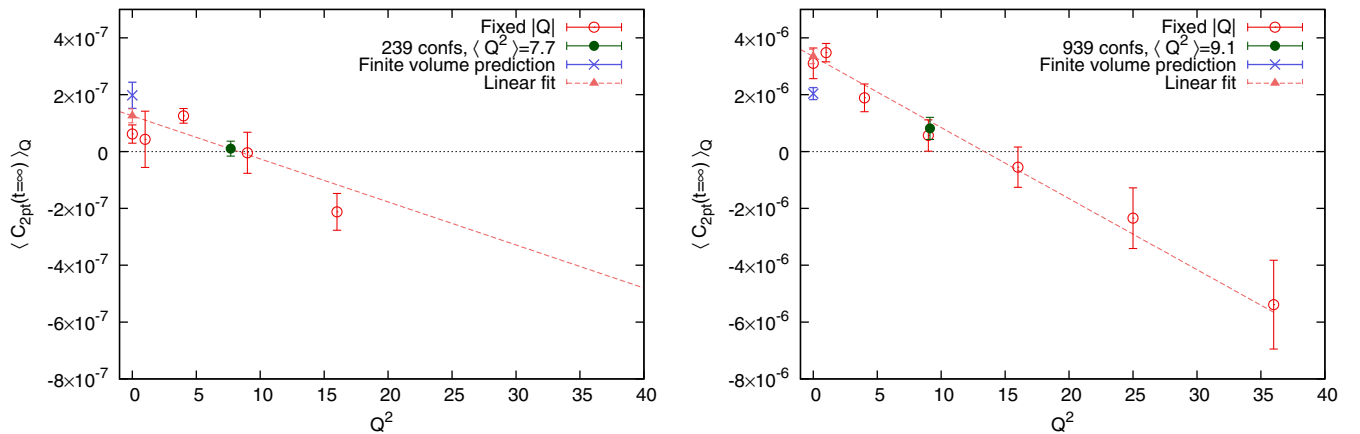

FIG. 6 (color online). The constant part of the naive zero-momentum η' two-point function for each topological sector, for Set A (left panel) and Set S (right panel). The green solid circles were obtained using all configurations. We found $\langle Q^2 \rangle \approx 7.7$ for Set A and $\langle Q^2 \rangle \approx 9.1$ for Set S. The $Q = 0$ finite volume predictions [blue crosses, Eqs. (17) and (15)] were calculated using $\chi_t = \langle Q^2 \rangle / V_4$ and slopes α, determined via Eq. (18). The dashed pink lines are linear fits to the fixed $|Q|$ data.

The details of the improved method are as follows. Noting that the Q^2 term in Eq. (14) comes from the disconnected part of the two-point function, we replace this contribution to the two-point function $D_{ab}(t)$ [see Eq. (B5) of Appendix B] by

$$D_{ab}(t) = \frac{a^4}{V_4} \sum_{t_0/a=0}^{T/a-1} C^a_{1\,pt}(t+t_0) C^b_{1\,pt}(t_0) \mapsto \tilde{D}_{ab}(t)$$

$$\equiv D_{ab}(t) - \frac{a^5}{V_4 T} \sum_{t_1/a,t_2/a=0}^{T/a-1} C^a_{1\,pt}(t_1) C^b_{1\,pt}(t_2), \quad (19)$$

where $p = 0$ is understood. We perform this subtraction on a configuration by configuration basis, shifting the correlator on different configurations by different values. This results in a "wrong" expectation value of D (and thus of $C^{\eta'}_{2\,pt}$) but the subtraction does not affect its t dependence. The resulting two-point function should approximately reproduce the behavior Eqs. (15) and (17) of the $Q = 0$ sector. Note that the cancellation cannot be perfect since, instead of subtracting $\langle \sum_t C_{1\,pt}(t) \rangle^2_Q$ within each fixed topology sector, in Eq. (19) we subtract $\langle [\sum_t C_{1\,pt}(t)]^2 \rangle$, thereby neglecting fluctuations of $\sum_t C_{1\,pt}(t)$ about αQ.

We remark that even on ensembles with the correct distribution of the topological charge we recommend to subtract this constant term from D, (approximately) normalizing this to the $Q = 0$ behavior, Eqs. (15) and (17), since this construction, as we will see below, significantly improves the signal over noise ratio.

Replacing $D_{ab}(t)$ with $\tilde{D}_{ab}(t)$ in $C^{ij}_{2\,pt}(t)$, $i,j = 1, 8$, as advertised above, we obtain modified two-point functions $\tilde{C}^{ij}_{2\,pt}(t)$ [see Eqs. (B1)–(B4)],

$$\tilde{C}^{88}_{2\,pt} = \frac{1}{3}(C_{ll} + C_{ss} - 2\tilde{D}_{ll} - 2\tilde{D}_{ss} + 2\tilde{D}_{ls} + 2\tilde{D}_{sl}), \quad (20)$$

$$\tilde{C}^{11}_{2\,pt} = \frac{1}{3}(2C_{ll} + C_{ss} - 4\tilde{D}_{ll} - \tilde{D}_{ss} - 2\tilde{D}_{ls} - 2\tilde{D}_{sl}), \quad (21)$$

$$\tilde{C}^{18}_{2\,pt} = (\tilde{C}^{81}_{2\,pt}(t))^*$$
$$= \frac{\sqrt{2}}{3}(C_{ll} - C_{ss} - 2\tilde{D}_{ll} + \tilde{D}_{ss} + 2\tilde{D}_{ls} - \tilde{D}_{sl}), \quad (22)$$

where C_{ab} is a connected two-point function with flavor $a, b = l, s$ and we have suppressed the t dependence. Each modified two-point function still approximately reproduces the constant term Eq. (15). Solving the generalized eigenvalue problem, we obtain eigenvectors $(\cos \tilde{\theta}, -\sin \tilde{\theta})^T$ and $(\sin \tilde{\theta}', \cos \tilde{\theta}')^T$. It is convenient to write the two-point functions in matrix notation,

$$\begin{pmatrix} \langle \tilde{C}^{\eta}_{2\,pt}(t) \rangle & 0 \\ 0 & \langle \tilde{C}^{\eta'}_{2\,pt}(t) \rangle \end{pmatrix}$$

$$= U(\tilde{\theta}, \tilde{\theta}') \begin{pmatrix} \langle \tilde{C}^{88}_{2\,pt}(t) \rangle & \langle \tilde{C}^{81}_{2\,pt}(t) \rangle \\ \langle \tilde{C}^{18}_{2\,pt}(t) \rangle & \langle \tilde{C}^{11}_{2\,pt}(t) \rangle \end{pmatrix} U^T(\tilde{\theta}, \tilde{\theta}'), \quad (23)$$

where

$$U(\tilde{\theta}, \tilde{\theta}') \equiv \begin{pmatrix} \cos \tilde{\theta} & -\sin \tilde{\theta} \\ \sin \tilde{\theta}' & \cos \tilde{\theta}' \end{pmatrix}. \quad (24)$$

The modified two-point functions of the physical interpolators at large times behave as

$$\langle \tilde{C}^{\eta}_{2\,pt}(t) \rangle = A_\eta(\exp[-E_\eta t] + \exp[-E_\eta(T-t)]) + \beta_\eta, \quad (25)$$

$$\langle \tilde{C}^{\eta'}_{2\,pt}(t) \rangle = A_{\eta'}(\exp[-E_{\eta'} t] + \exp[-E_{\eta'}(T-t)]) + \beta_{\eta'}. \quad (26)$$

From this we can obtain the constants β_η and $\beta_{\eta'}$. At the SU(3) symmetric point, where $\tilde{\theta} = \tilde{\theta}' = 0$, we obtain the mass of the η' from Eq. (26) alone. In this case $\eta = \eta_8$ does not contain disconnected contributions and $\beta_\eta = 0$.

At the flavor nonsymmetric point, the removal of the constant part is more involved. By inverting Eq. (23) we can obtain the contributions to β_η and $\beta_{\eta'}$ from the two-point functions in the octet-singlet basis. We define improved two-point functions for $p = 0$, subtracting these:

$$\begin{pmatrix} \langle C^{88}_{2\,pt}(t) \rangle & \langle C^{81}_{2\,pt}(t) \rangle \\ \langle C^{18}_{2\,pt}(t) \rangle & \langle C^{11}_{2\,pt}(t) \rangle \end{pmatrix}_{\text{improved}}$$

$$= \begin{pmatrix} \langle \tilde{C}^{88}_{2\,pt}(t) \rangle & \langle \tilde{C}^{81}_{2\,pt}(t) \rangle \\ \langle \tilde{C}^{18}_{2\,pt}(t) \rangle & \langle \tilde{C}^{11}_{2\,pt}(t) \rangle \end{pmatrix}$$

$$- U^{-1}(\tilde{\theta}, \tilde{\theta}') \begin{pmatrix} \beta_\eta & 0 \\ 0 & \beta_{\eta'} \end{pmatrix} (U^{-1})^T(\tilde{\theta}, \tilde{\theta}'). \quad (27)$$

Solving the generalized eigenvalue problem for the improved two-point functions, we then obtain the masses and improved θ and θ' angles that we will use to construct the physical interpolators at $p = 0$.

The effective masses of the η' before and after the improvement are plotted in Fig. 7 for the two ensembles. The results obtained from the naive fit with a constant are also shown. For very large statistics there should be no difference between the naive effective mass and the other two definitions; however, as we have already discussed above, Set S showed a nonrealistic distribution of the topological charge. The improved method gives the best signals and shows clear plateaus.
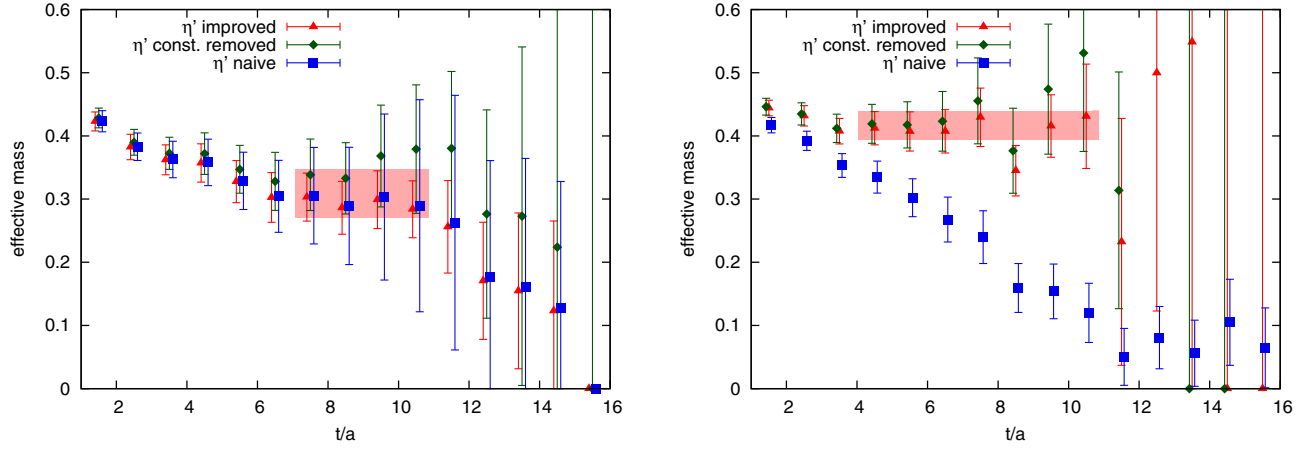
FIG. 7 (color online). Effective mass of the η', before and after the improvement, for Set A (left panel) and Set S (right panel). Results are shown for three cases (a) using the naive η' two-point correlators, $C_{2\,\mathrm{pt}}^{\eta^{(\prime)}}$, of Eq. (8) (blue squares), (b) using the naive correlators after removing the constant term (green diamonds) and (c) using the improved two-point functions, removing the constant part Eq. (26) for Set S, and solving the generalized eigenvalue problem for Eq. (27) for Set A (red triangles).

The method we presented here was motivated by the inadequate sampling of the topological charge on one of our ensembles. However, it is generally applicable to calculations of disconnected contributions to light pseudoscalar two-point functions. The improved two-point functions show reduced fluctuations, at the price of a constant term that needs to be fitted. In spite of this additional parameter, the extracted masses are more precise than they are using the naive approach.

C. Mixing of the η and η' mesons in the octet-singlet basis

In addition to the mass, the mixing angles between the physical η' and η states and the octet-singlet basis are also of phenomenological importance. We restrict ourselves to Set A since at the SU(3) flavor symmetric point (Set S) there is no such mixing and $\eta' = \eta_1$, $\eta = \eta_8 = \pi$. We define the two leading distribution amplitudes

$$A_{j\eta^{(\prime)}} \equiv \langle 0|\mathcal{O}_j^{\mathrm{local}}|\eta^{(\prime)}\rangle, \tag{28}$$

where $\mathcal{O}_j^{\mathrm{local}}$ is a local singlet ($j = 1$) or octet ($j = 8$) interpolator projected onto zero momentum, and use the following parametrizations for which the renormalization factors of $\mathcal{O}_j^{\mathrm{local}}$ cancel [26] (see also [36] and references therein[4]):

$$\frac{A_{8\eta'}}{A_{8\eta}} = \tan\theta_8, \qquad \frac{A_{1\eta}}{A_{1\eta'}} = -\tan\theta_1, \qquad \tan^2\bar{\theta} = \tan\theta_8\tan\theta_1. \tag{29}$$

To obtain these amplitudes, we use the asymptotic behavior at large times t of smeared source to local (point) sink two-point functions at zero momentum[5]

$$\langle C_{2\,\mathrm{pt},\mathrm{sm}\to\mathrm{pt}}^{j\eta^{(\prime)}}(t)\rangle = \langle 0|\mathcal{O}_j^{\mathrm{local}}(t)\mathcal{O}_{\eta^{(\prime)}}^\dagger(0)|0\rangle \to \frac{A_{j\eta^{(\prime)}}Z_{\eta^{(\prime)}}}{2M_{\eta^{(\prime)}}}$$

$$\times (\exp[-M_{\eta^{(\prime)}}t] + \exp[-M_{\eta^{(\prime)}}(T-t)])$$

$$+ \beta_{j\eta^{(\prime)}}, \tag{30}$$

where $Z_{\eta^{(\prime)}} = \langle\eta^{(\prime)}|\mathcal{O}_{\eta^{(\prime)}}^\dagger|0\rangle$ [see Eq. (36) below] can be obtained from the smeared-smeared two-point function. The physical η or η' state is created by $\mathcal{O}_{\eta^{(\prime)}}^\dagger$, for which we use the improved θ or θ' parameters obtained from the smeared-smeared correlators in the previous subsection. Note that these angles depend on our choice of smearing and—unlike the mixing angles discussed below—are not properties of the physical states alone. Using the mixing angles θ and θ' we build the improved two point functions

$$\langle \tilde{C}_{2\,\mathrm{pt},\mathrm{sm}\to\mathrm{pt}}^{j\eta}(t)\rangle = \cos\theta\langle\tilde{C}_{2\,\mathrm{pt},\mathrm{sm}\to\mathrm{pt}}^{j8}(t)\rangle$$

$$- \sin\theta\langle\tilde{C}_{2\,\mathrm{pt},\mathrm{sm}\to\mathrm{pt}}^{j1}(t)\rangle, \tag{31}$$

$$\langle \tilde{C}_{2\,\mathrm{pt},\mathrm{sm}\to\mathrm{pt}}^{j\eta'}(t)\rangle = \sin\theta'\langle\tilde{C}_{2\,\mathrm{pt},\mathrm{sm}\to\mathrm{pt}}^{j8}(t)\rangle$$

$$+ \cos\theta'\langle\tilde{C}_{2\,\mathrm{pt},\mathrm{sm}\to\mathrm{pt}}^{j1}(t)\rangle. \tag{32}$$

Both sides of the above equations may contain constant contributions, due to the replacement $C \mapsto \tilde{C}$ coming from the improved method.

---

[4]Note that in Ref. [36], decay constants $f_{j\eta^{(\prime)}}$ are used instead of the $A_{j\eta^{(\prime)}}$, which are defined as $\langle 0|A_j^\mu|\eta^{(\prime)}\rangle = ip^\mu f_{j\eta^{(\prime)}}$ with axial octet and singlet currents A_j^μ.

[5]Note that we use the improved method outlined in the previous subsection, Eqs. (20)–(22), replacing the disconnected contribution as in Eq. (19), this time also for smeared-point two-point functions. Therefore, we have to allow for constant contributions that we denote as $\beta_{j\eta^{(\prime)}}$.

TABLE III.   The mixing angles θ_8, θ_1 and $\bar{\theta}$ in degrees for Set A. The improved and unimproved values were obtained using $\tilde{C}^{j\eta^{(\prime)}}_{2\mathrm{pt},\mathrm{sm}\to\mathrm{pt}}(t)$ and $C^{j\eta^{(\prime)}}_{2\mathrm{pt},\mathrm{sm}\to\mathrm{pt}}(t)$, respectively. The first errors are statistical and the second quantify the uncertainty from the choice of the fit range.

	Improved, $\beta_{j\eta^{(\prime)}} \neq 0$	Unimproved, $\beta_{j\eta^{(\prime)}} \neq 0$	Unimproved, $\beta_{j\eta^{(\prime)}} = 0$
θ_8	$-10.9(1.5)_{\mathrm{stat}}(0.5)_{\mathrm{fit}}$	$-10.9(1.5)_{\mathrm{stat}}(0.4)_{\mathrm{fit}}$	$-10.5(1.1)_{\mathrm{stat}}(0.2)_{\mathrm{fit}}$
θ_1	$-5.5(1.5)_{\mathrm{stat}}(1.2)_{\mathrm{fit}}$	$-5.5(1.5)_{\mathrm{stat}}(1.2)_{\mathrm{fit}}$	$-7.1(1.2)_{\mathrm{stat}}(1.3)_{\mathrm{fit}}$
$\bar{\theta}$	$-7.7(0.9)_{\mathrm{stat}}(0.8)_{\mathrm{fit}}$	$-7.7(0.9)_{\mathrm{stat}}(0.7)_{\mathrm{fit}}$	$-8.6(0.9)_{\mathrm{stat}}(0.9)_{\mathrm{fit}}$

TABLE IV.   The distribution amplitudes for Set A normalized with respect to A_π, using the three different methods. The (unknown) renormalization factor exactly cancels from the octet ratios and is partially canceled in the singlet ratios.

	Improved, $\beta_{j\eta^{(\prime)}} \neq 0$	Unimproved, $\beta_{j\eta^{(\prime)}} \neq 0$	Unimproved, $\beta_{j\eta^{(\prime)}} = 0$
$A_{8\eta}/A_\pi$	$1.124(14)_{\mathrm{stat}}(04)_{\mathrm{fit}}$	$1.124(14)_{\mathrm{stat}}(04)_{\mathrm{fit}}$	$1.120(14)_{\mathrm{stat}}(03)_{\mathrm{fit}}$
$A_{1\eta}/A_\pi$	$0.058(24)_{\mathrm{stat}}(12)_{\mathrm{fit}}$	$0.058(24)_{\mathrm{stat}}(12)_{\mathrm{fit}}$	$0.082(19)_{\mathrm{stat}}(08)_{\mathrm{fit}}$
$A_{8\eta'}/A_\pi$	$-0.216(31)_{\mathrm{stat}}(11)_{\mathrm{fit}}$	$-0.216(31)_{\mathrm{stat}}(11)_{\mathrm{fit}}$	$-0.207(22)_{\mathrm{stat}}(39)_{\mathrm{fit}}$
$A_{1\eta'}/A_\pi$	$0.60(13)_{\mathrm{stat}}(20)_{\mathrm{fit}}$	$0.60(13)_{\mathrm{stat}}(21)_{\mathrm{fit}}$	$0.65(12)_{\mathrm{stat}}(17)_{\mathrm{fit}}$

We fit $\langle \tilde{C}^{j\eta^{(\prime)}}_{2\,\mathrm{pt},\mathrm{sm}\to\mathrm{pt}}(t) \rangle$, fixing the mass $M_{\eta^{(\prime)}}$ to the value we determined previously, leaving $A_{j\eta^{(\prime)}}$ and $\beta_{j\eta^{(\prime)}}$ as free parameters. The resulting angles θ_1, θ_8 and $\bar{\theta}$ [see Eq. (29)] are given in Table III. The first error is statistical, while the second one is an estimate of the systematics from the choice of the fit range and was obtained varying this by ± 1 time slices. Note that, since both $\tan\theta_8$ and $\tan\theta_1$ are negative, we also adopted a negative value for $\tan\bar{\theta}$. θ_8 was found to differ from θ_1 (and hence from $\bar{\theta}$): two angles are needed to connect the physical states to the octet-singlet basis, indicating the relevance of higher Fock states. A phenomenological estimate used in Ref. [36] also gives two mixing angles, $\theta_8 = -21.2(1.6)^\circ$ and $\theta_1 = -9.2(1.7)^\circ$, where the errors are solely experimental and no systematic errors are included. In the lattice study of Ref. [25] a single mixing angle $-14.1(2.8)^\circ$ was obtained, relative to the octet-singlet basis, after extrapolating to the physical point. This is in the middle between the phenomenological θ_1 and θ_8 values. The ratio θ_8/θ_1 of Ref. [36] is consistent with our result; however, both our angles come out a factor of 2 smaller than in that analysis. This is not surprising since we start from the flavor-symmetric point where $\theta_8 = \theta_1 = 0$, while Set A corresponds to a quark mass ratio $m_s/m_l \approx 2.8$, still quite far away from the physical point $m_s/m_l \approx 25$. A monotonous extrapolation would indeed suggest larger values of $|\theta_j|$ for physical m_s/m_l.

Another interesting combination is ratios of the $A_{j\eta^{(\prime)}}$ amplitudes to a similar distribution amplitude for the pion

$$\frac{A_{j\eta^{(\prime)}}}{A_\pi} \quad \text{with} \quad A_\pi \equiv \langle 0 | \mathcal{O}^{\mathrm{local}}_\pi | \pi \rangle, \qquad (33)$$

where $\mathcal{O}^{\mathrm{local}}_\pi$ is the local pion interpolator. Note that the renormalization factors only cancel exactly for the ratios

$A_{8\eta^{(\prime)}}/A_\pi$ while in the singlet case this is violated at two-loop order in perturbation theory. In Table IV, we list the values (in the left column). The octet component of the η meson is enhanced, relative to the flavor-symmetric case while the singlet η' distribution amplitude is much smaller than that for the pion. Note that the negative value of $A_{8\eta'}$ signals an octet-admixture to η' much bigger than the singlet component of η, which is another manifestation of the result $|\theta_8| > |\theta_1|$.

For completeness, we also determined the angles and ratios using the (unimproved) $\langle C^{j\eta^{(\prime)}}_{2\,\mathrm{pt},\mathrm{sm}\to\mathrm{pt}}(t) \rangle$ with both $\beta_{j\eta^{(\prime)}} = 0$ and $\beta_{j\eta^{(\prime)}} \neq 0$ in the fit function. The results are included in Tables III and IV for comparison. The three determinations are broadly consistent for both quantities. We see no significant reduction in the statistical errors between the unimproved/improved $\beta_{j\eta^{(\prime)}} \neq 0$ cases. This may be due to the use of the same (improved) θ and θ' to construct the physical states or that the assumption of small fluctuations of $\sum_t C_{1\mathrm{pt}}(t)$ around the topological charge [see the argument below Eq. (19)] may be less valid for the local one-point loop. The naive (unimproved $\beta_{j\eta^{(\prime)}} = 0$) errors are slightly smaller since the fit parameters $\beta_{j\eta^{(\prime)}}$ are fixed. The discussion of the previous subsection, however, suggests that due to the coupling between the disconnected loop and the slowly moving topological charge it is safer to allow for such constants.

IV. DETERMINATION OF THE SEMILEPTONIC FORM FACTORS

Having obtained the η and η' interpolators, we are now in the position to calculate the $D_s \to \eta \ell \bar{\nu}_\ell$ and $D_s \to \eta' \ell \bar{\nu}_\ell$ semileptonic decay form factors $f_0(q^2)$. We discuss the relevant matrix elements and our methods to compute these, before we present and discuss our results on the form factors.
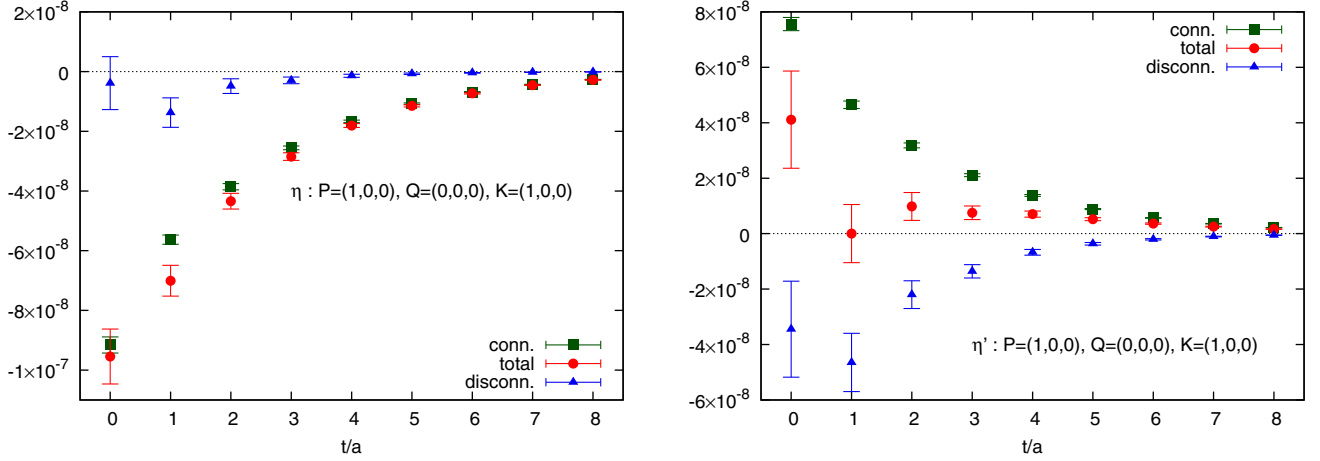
FIG. 8 (color online).   Connected (green squares) and disconnected (blue triangles) contributions to the total three-point functions (red circles) for $D_s \to \eta$ (left panel) and $D_s \to \eta'$ (right panel) matrix elements for Set A with $t_{\text{sep}} = 8a$. The D_s is located at $t = 0$ and the $\eta^{(\prime)}$ is at $t = 8a$. The momenta are in the lattice units: $(\boldsymbol{P}, \boldsymbol{Q}, \boldsymbol{K}) = (\boldsymbol{p}, \boldsymbol{q}, \boldsymbol{k}) \times L/(2\pi)$.

A. Matrix elements

The matrix elements needed to study the decays $D_s \to \eta^{(\prime)} \ell \bar{\nu}_\ell$ are obtained from the following three-point functions:

$$\langle C_{3\text{pt}}^{D_s \to \eta^{(\prime)}}(t, \boldsymbol{p}, \boldsymbol{k}; t_{\text{sep}}) \rangle = \langle 0 | \mathcal{O}_{\eta^{(\prime)}}(\boldsymbol{k}, t_{\text{sep}}) S(\boldsymbol{0}, t) \mathcal{O}_{D_s}^\dagger(\boldsymbol{p}, 0) | 0 \rangle, \quad (34)$$

where we used smeared interpolators $\mathcal{O}_{D_s}$ and $\mathcal{O}_{\eta^{(\prime)}}$ for both the D_s and the $\eta^{(\prime)}$, respectively. S is the local scalar current in position space. It can also be averaged over the spatial

volume (multiplying by the phases $e^{i\boldsymbol{q} \cdot (\boldsymbol{x} - \boldsymbol{x}_0)}$), to increase statistics. We detail the computation methods for both the connected and the disconnected contributions to the three-point functions in Appendix C. Figure 8 shows the full three-point function and the contributions from connected and disconnected fermion loop diagrams. It is interesting to note that the magnitude of the disconnected contributions is large, especially for the decay to η'. Not surprisingly, the statistical error of the three-point function mainly comes from the disconnected part.

The three-point functions have the following spectral decomposition:

$$\langle C_{3\text{pt}}^{D_s \to \eta^{(\prime)}}(t, \boldsymbol{p}, \boldsymbol{k}; t_{\text{sep}}) \rangle = \frac{Z_{\eta^{(\prime)}}}{2E_{\eta^{(\prime)}}} \frac{Z_{D_s}}{2E_{D_s}} \langle \eta^{(\prime)}(\boldsymbol{k}) | S(\boldsymbol{0}) | D_s(\boldsymbol{p}) \rangle \exp\left[-E_{D_s}(T-t) - E_{\eta^{(\prime)}}(T - (t_{\text{sep}} - t))\right]$$
$$+ \frac{Z_{\eta^{(\prime)*}}}{2E_{\eta^{(\prime)*}}} \frac{Z_{D_s}}{2E_{D_s}} \langle \eta^{(\prime)*}(\boldsymbol{k}) | S(\boldsymbol{0}) | D_s(\boldsymbol{p}) \rangle \exp\left[-E_{D_s}(T-t) - E_{\eta^{(\prime)*}}(T - (t_{\text{sep}} - t))\right]$$
$$+ \frac{Z_{\eta^{(\prime)}}}{2E_{\eta^{(\prime)}}} \frac{Z_{D_s^*}}{2E_{D_s^*}} \langle \eta^{(\prime)}(\boldsymbol{k}) | S(\boldsymbol{0}) | D_s^*(\boldsymbol{p}) \rangle \exp\left[-E_{D_s^*}(T-t) - E_{\eta^{(\prime)}}(T - (t_{\text{sep}} - t))\right]$$
$$+ \frac{Z_{\eta^{(\prime)*}}}{2E_{\eta^{(\prime)*}}} \frac{Z_{D_s^*}}{2E_{D_s^*}} \langle \eta^{(\prime)*}(\boldsymbol{k}) | S(\boldsymbol{0}) | D_s^*(\boldsymbol{p}) \rangle \exp\left[-E_{D_s^*}(T-t) - E_{\eta^{(\prime)*}}(T - (t_{\text{sep}} - t))\right] + \cdots, \quad (35)$$

where $*$ indicates the first excited states and we have neglected contributions from even higher excitations. $Z_{X^{(*)}}$ is the amplitude of the state with $X = D_s$, η and η'. For brevity we suppress the momentum dependence of $Z_{X^{(*)}} = Z_{X^{(*)}}(\boldsymbol{p})$ and $E_{X^{(*)}} = E_{X^{(*)}}(\boldsymbol{p})$. The first term on the right-hand side contains the ground state to ground state matrix element that we are interested in.

Note that the phase of the state X is arbitrary and we choose it such that we have a real positive amplitude

$$Z_X = \langle X | \mathcal{O}_X^\dagger | 0 \rangle > 0. \quad (36)$$

This means that the matrix elements $\langle D_s(\boldsymbol{p}) | S(\boldsymbol{0}) | \eta^{(\prime)}(\boldsymbol{k}) \rangle$ can be negative[6] and, indeed, we obtained negative values

---

[6]Charge conjugation invariance guarantees the matrix element is real in coordinate space, and then parity invariance $\langle D_s(\boldsymbol{p}) | S(\boldsymbol{0}) | \eta^{(\prime)}(\boldsymbol{k}) \rangle = \langle D_s(-\boldsymbol{p}) | S(\boldsymbol{0}) | \eta^{(\prime)}(-\boldsymbol{k}) \rangle$ gives a real three-point function in momentum space.

for the η. Since the sign of the matrix element is not physical, in the following we use its modulus.[7]

In order to determine the ground state to ground state matrix element reliably, it is important to take into account the excited state contributions to the three-point function. One way to do this is to use a large sink-source separation so that the excited state contributions are small. However, this is not possible in the current case because the statistical error grows rapidly (due to the disconnected terms), even for relatively small time separations. We need to employ an alternative approach.

First we obtain E_X and Z_X by fitting the two-point function

$$\langle C_X^{2\mathrm{pt}}(\boldsymbol{p}, t)\rangle = \frac{|Z_X|^2}{2E_X}\left(\exp[-E_X t] + \exp[-E_X(T - t)]\right) + \frac{|Z_{X^*}|^2}{2E_{X^*}}\left(\exp[-E_{X^*} t] + \exp[-E_{X^*}(T - t)]\right) + \cdots, \qquad (37)$$

using a functional form given by the first term, at sufficiently large t. The energy gap, $\Delta E_X = E_{X^*} - E_X$, is then determined by fitting the combination

$$\frac{\langle C_X^{2\mathrm{pt}}(t, \boldsymbol{p})\rangle}{\frac{|Z_X|^2}{2E_X}\left(\exp[-E_X t] + \exp[-E_X(T - t)]\right)} - 1 \qquad (38)$$

to the form $a_X \exp(-\Delta E_X t)$, where not only ΔE_X but also the amplitudes a_X depend on the momentum $\boldsymbol{p}$. To extract the matrix element, $\langle \eta^{(\prime)}(\boldsymbol{k})|S(\boldsymbol{0})|D_s(\boldsymbol{p})\rangle$, we compute the ratio

$$R(t) = \frac{\langle C_{3\mathrm{pt}}^{D_s \to \eta^{(\prime)}}(t, \boldsymbol{p}, \boldsymbol{k}; t_{\mathrm{sep}})\rangle}{\frac{Z_{D_s}}{2E_{D_s}}\left(\exp\left[-E_{D_s} t\right] + \exp\left[-E_{D_s}(T - t)\right]\right)\frac{Z_{\eta^{(\prime)}}}{2E_{\eta^{(\prime)}}}\left(\exp\left[-E_{\eta^{(\prime)}}(t_{\mathrm{sep}} - t)\right] + \exp\left[-E_{\eta^{(\prime)}}(T - (t_{\mathrm{sep}} - t))\right]\right)} \qquad (39)$$

and use the fit function

$$R(t) = c + A_1 \exp\left[-\Delta E_{D_s} t\right] + A_2 \exp\left[-\Delta E_{\eta^{(\prime)}}(t_{\mathrm{sep}} - t)\right], \qquad (40)$$

where $c = \langle \eta^{(\prime)}(\boldsymbol{k})|S(\boldsymbol{0})|D_s(\boldsymbol{p})\rangle$. Whenever the two-point function had a small overlap with the excited state and we were unable to extract $\Delta E_{\eta^{(\prime)}}$, we only employed the first two terms of Eq. (40).

We generated three different data sets with $t_{\mathrm{sep}}/a = 8, 10, 16$ and fitted these simultaneously. For the η at the SU(3) flavor symmetric point, which has no disconnected contributions, we also generated $t_{\mathrm{sep}}/a = 24$ data. For some momentum combinations only a subset of the available data was used in the fits, either because of the data being too noisy (for $t_{\mathrm{sep}}/a = 24$) or because contributions from the second or higher excited states were significant (for $t_{\mathrm{sep}}/a = 8$). Details of the chosen fit ranges are listed in Tables IX–XII of Appendix D and typical examples of the fits using Eq. (40) are shown in Fig. 9.

Again, we used correlated fits and varied the fit region to assess systematic uncertainties. The changes of the fit parameter values were found to be well within the statistical errors. The only exception was for the three-point function involving the η meson at the SU(3) flavor symmetric point. In this case, the statistical errors were small such that the systematic uncertainties became relevant and we opted for employing an uncorrelated fit and a fit range that resulted in errors large enough to encompass the systematics.

B. Results

The results for the form factor, derived from the matrix elements using Eq. (2), are listed in Tables IX–XII for the momentum ranges $\boldsymbol{P}^2 \leq 4$ and $\boldsymbol{K}^2 \leq 3$ in lattice units $[\boldsymbol{P} = \boldsymbol{p} \times L/(2\pi)]$. Note that we defined the four-momentum transfer q^2 as

$$q^2 \equiv (E_{D_s}(\boldsymbol{p}) - E_{\eta^{(\prime)}}(\boldsymbol{k}))^2 - (\boldsymbol{p} - \boldsymbol{k})^2, \qquad (41)$$

where the energies of the D_s and $\eta^{(\prime)}$ states are listed in Tables VII and VIII of Appendix D and depicted in Fig. 2. The values at nonzero momenta were determined directly, without using a dispersion relation. The dependence of $f_0(q^2)$ on q^2 is shown in Fig. 10.

We used a one pole ansatz to interpolate the data to $q^2 = 0$,

$$f_0(q^2) = \frac{f_0(0)}{1 - bq^2}. \qquad (42)$$

---

[7]Note, however, that relative signs are relevant for studies of flavor mixing angles in decays. This is similar to the connection of the sign of the distribution amplitude ratio $A_{8\eta'}/A_\pi$ to the sign of the respective mixing angle θ_8.
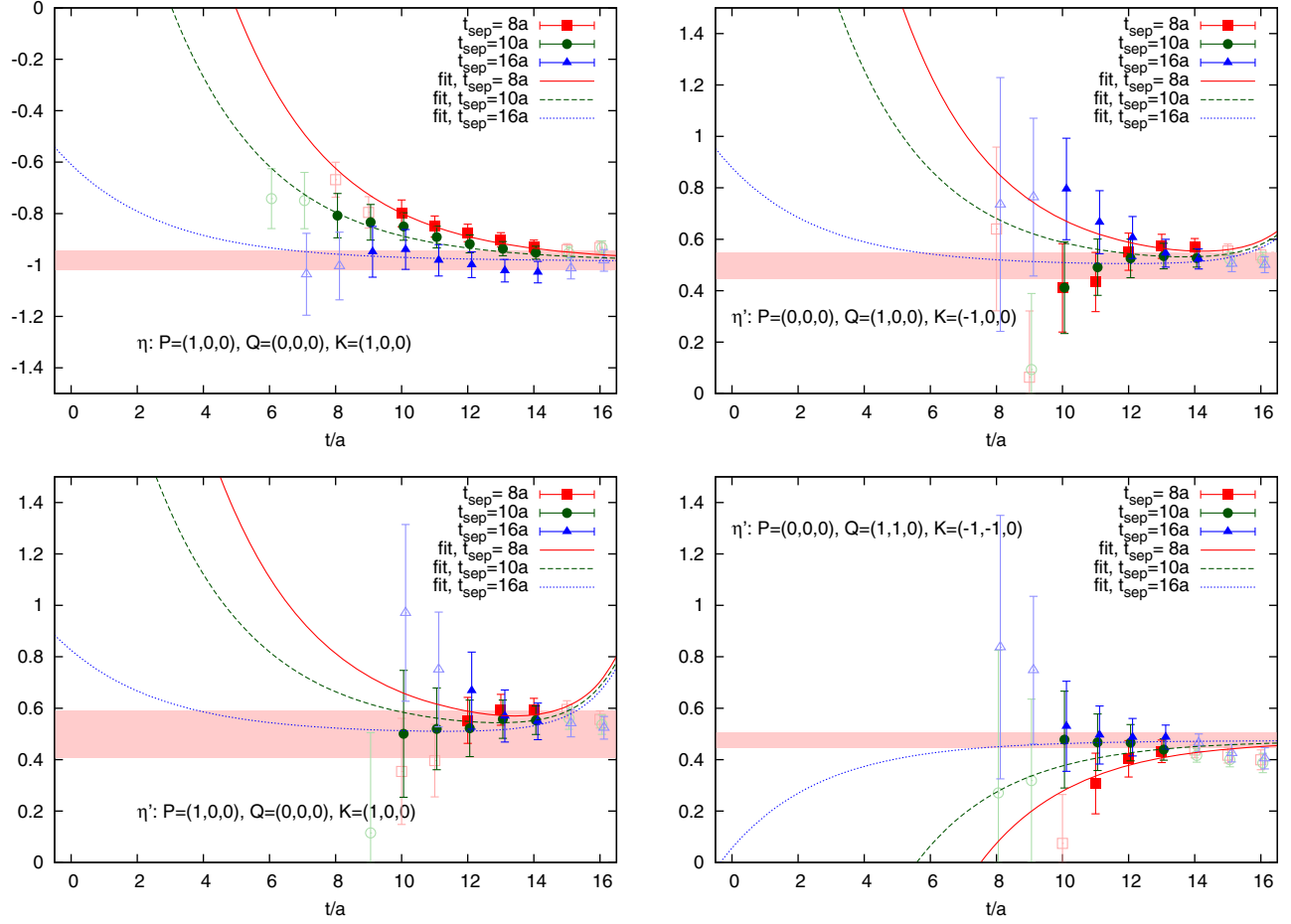
FIG. 9 (color online).   Typical examples of fitting $R(t)$ to Eq. (40), to extract $\langle \eta^{(')}(\boldsymbol{k})|S(\boldsymbol{0})|D_s(\boldsymbol{p})\rangle$, for Set A. The lower right plot depicts a fit to the first two terms of Eq. (40), while the others use all three terms. The D_s meson is always located at $t/a = 16$, while the η or η' is located at $t/a = 8$ ($t_{sep}/a = 8$), $t/a = 6$ ($t_{sep}/a = 10$) and $t = 0$ ($t_{sep}/a = 16$). Data points with open symbols were omitted from the fits. The red bands indicate the values of the matrix elements obtained from the fit. The momenta are in the lattice units: $(\boldsymbol{P}, \boldsymbol{Q}, \boldsymbol{K}) = (\boldsymbol{p}, \boldsymbol{q}, \boldsymbol{k}) \times L/(2\pi)$.
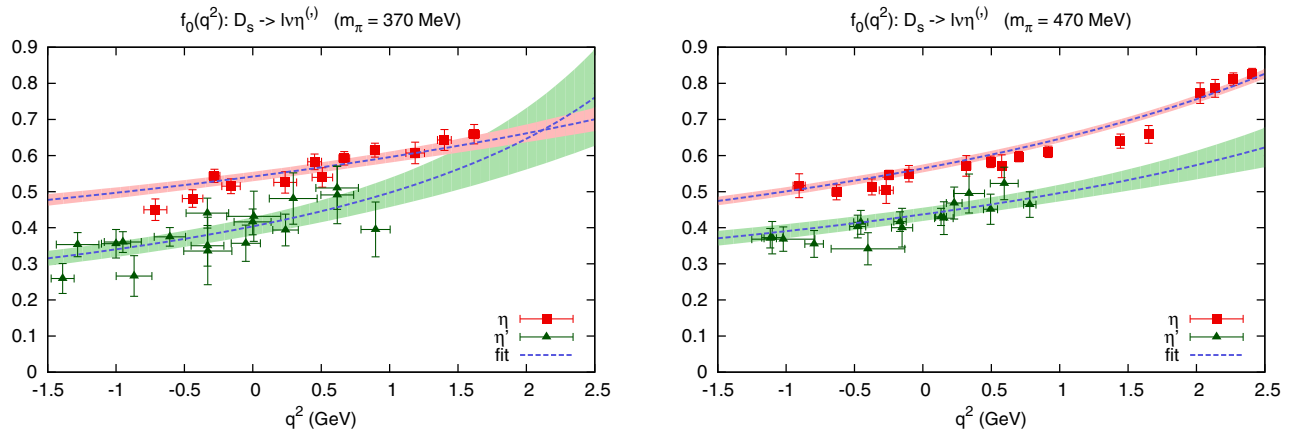

FIG. 10 (color online).   The scalar form factor $f_0(q^2)$ for $D_s \to \eta^{(')}\ell\bar{\nu}_\ell$. The errors are statistical only and the dashed lines indicate the fits to the form factors using the parametrization $f_0(q^2) = f_0(0)/(1 - bq^2)$. On the left are the results for $M_\pi \approx 370$ MeV (Set A) and on the right for $M_\pi \approx 470$ MeV (Set S).

TABLE V. Parameters $f_0(0)$ and b obtained from a fit $f_0(q^2) = f_0(0)/(1 - bq^2)$. The coefficient β corresponds to an equivalent fit using the BK [37] parametrization. The light cone QCD sum rule results are taken from Ref. [4].

Set	Meson	$f_0(q^2 = 0)$	b (GeV)$^{-2}$	β
S	η	0.564(11)	0.127(06)	1.70(08)
	η'	0.437(18)	0.119(23)	1.81(35)
A	η	0.542(13)	0.090(14)	2.35(36)
	η'	0.404(25)	0.188(32)	1.13(19)
LCSRs (at M_π^{phys})	η	0.432(33)	$\cdots$	$\cdots$
	η'	0.520(80)	$\cdots$	$\cdots$

These curves are also shown in Fig. 10. The resulting values for $f_0(0)$ are listed in Table V. The parametrization of Becirević and Kaidalov (BK) [37] is frequently used in the literature too. For the scalar form factor, this is essentially the same parametrization as Eq. (42) but the location of the pole is normalized with respect to the vector meson mass $M_{D_s^*}$,[8]

$$f_0(q^2) = \frac{f_0(0)}{1 - x/\beta} \qquad (43)$$

with $x = q^2/M_{D_s^*}^2$. The values of β obtained from rescaling the parameter b above are also listed in Table V.

A comparison can be made with the values derived from light cone QCD sum rules (LCSRs) [4], displayed in Table V, where we assumed $f_+(q^2 = 0) = f_0(q^2 = 0)$. Encouragingly, the results are broadly consistent. We find $f_0(q^2 = 0)$ is larger for the η than for the η', independent of the quark mass, while for LCSRs the ordering cannot be resolved due to the large error for the η'. The ratios of the form factors $|f_+^{D_s \to \eta'}(0)|/|f_+^{D_s \to \eta}(0)| = |f_0^{D_s \to \eta'}(0)|/|f_0^{D_s \to \eta}(0)|$ are

$$0.775(032) \quad (\text{Set S}), \qquad 0.746(046) \quad (\text{Set A}),$$

$$1.20(17) \quad (\text{LCSRs}). \qquad\qquad\qquad\qquad (44)$$

A more detailed comparison would require an estimation of the dominant systematic uncertainties. These uncertainties are difficult to quantify in both studies, in the LCSRs case due to the approximations made, while in our study since we have a single lattice volume and lattice spacing. Considering our lightest pseudoscalar mass is around 370 MeV and $LM_\pi = 3.3$, extending the analysis to bigger volumes and smaller quark masses is important.

C. Outlook on phenomenology

The results given in the previous subsection do not allow for a direct determination of the widths $\Gamma(D_s^- \to \eta e^- \bar{\nu}_e)$

---

[8]This should not be confused with the excited state of the pseudoscalar meson which we also denoted by a ∗ in the previous subsection.

and $\Gamma(D_s^- \to \eta' e^- \bar{\nu}_e)$, since we computed $f_0(q^2)$ rather than $f_+(q^2)$ and used heavier-than-physical pion masses. Accordingly, a direct comparison to, for example, the ratio $\Gamma(D_s^- \to \eta' e^- \bar{\nu}_e)/\Gamma(D_s^- \to \eta e^- \bar{\nu}_e) = 0.36(14)$, as determined by the CLEO Collaboration [6], is not yet possible. However, invoking some model assumptions, a tentative comparison can be made, albeit at the price of introducing an essentially unquantifiable uncertainty.

We calculate the ratio

$$\frac{\Gamma(D_s^- \to \eta' e^- \bar{\nu}_e)}{\Gamma(D_s^- \to \eta e^- \bar{\nu}_e)} = \frac{\int_0^{(M_{D_s} - M_{\eta'})^2} \lambda_{D_s,\eta'}^{3/2}(q^2)|f_+^{D_s \to \eta'}(q^2)|^2 dq^2}{\int_0^{(M_{D_s} - M_\eta)^2} \lambda_{D_s,\eta}^{3/2}(q^2)|f_+^{D_s \to \eta}(q^2)|^2 dq^2},$$

$$(45)$$

where $\lambda_{H,P}(x)$ is the heavy-light kinematic factor

$$\lambda_{H,P}(x) = \frac{1}{4M_H^2}((M_H^2 + M_P^2 - x)^2 - 4M_H^2 M_P^2), \quad (46)$$

by replacing $f_+(q^2)$ with the Ball-Zwicky ansatz [38]

$$f_+^{\text{BZ}}(q^2) = f_0(0)\left(\frac{1}{1 - q^2/M_{D_s^*}^2}\right.$$
$$\left. + \frac{rq^2/M_{D_s^*}^2}{(1 - q^2/M_{D_s^*}^2)(1 - \alpha q^2/M_{D_s^*}^2)}\right) \quad (47)$$

and using a chirally extrapolated value of our lattice results for $f_0(0)$. $M_{D_s^*}, \alpha, r$ are taken from the literature. We choose to compute the ratio rather than the individual decay rates since systematics in the chiral extrapolation and the phenomenological parametrization of $f_+(q^2)$ partially cancel between the decay rates for η and η'.

Using the above parametrization only the ratio $f_0^{D_s \to \eta'}(0)/f_0^{D_s \to \eta}(0)$ enters in Eq. (45); thus we extrapolate our two values for the ratio, given in Eq. (44), linearly in M_π^2 to the physical mass point (see Fig. 11); this yields $f_0^{D_s \to \eta'}(0)/f_0^{D_s \to \eta}(0) = 0.705(120)(041)$, where the first uncertainty is statistical and the second one is systematic (taken as the difference between the central values at $M_\pi = 370$ MeV and 135 MeV). For $M_{D_s^*}$ we take the experimental value [29], and for α, r we use the central values determined in Ref. [4], with 50% uncertainties: $\alpha = 0.252(126)$ and $r = 0.284(142)$.

We vary α and r independently within the form factors $f_+^{D_s \to \eta}$ and $f_+^{D_s \to \eta'}$ and evaluate Eq. (45) assuming Gaussian distributions of the five parameters $f_0^{D_s \to \eta'}(0)/f_0^{D_s \to \eta}(0)$, r_η, α_η, $r_{\eta'}$ and $\alpha_{\eta'}$ within the respective errors given above. In the right panel of Fig. 11 the resulting histogram is shown. We find
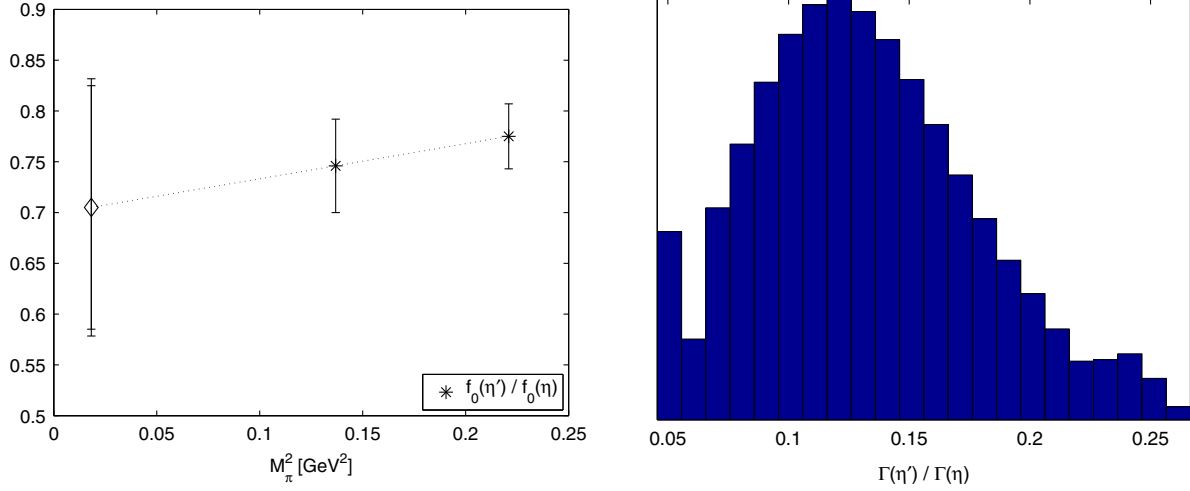
FIG. 11 (color online).   Left: Extrapolation of the ratio $f_0^{D_s\to\eta\prime}(0)/f_0^{D_s\to\eta}(0)$ to the physical pion mass. The inner error bar of the extrapolated ratio is statistical, and the outer one includes systematics (see text for details). Right: Histogram of the ratio Eq. (45), varying the ratio $f_0^{D_s\to\eta\prime}(0)/f_0^{D_s\to\eta}(0)$ within its errors as well as the parameters r and α within Eq. (47) for the decays into η and $\eta\prime$.

$$\frac{\Gamma(D_s^- \to \eta\prime e^- \bar{\nu}_e)}{\Gamma(D_s^- \to \eta e^- \bar{\nu}_e)} = 0.128^{+51}_{-42}, \qquad (48)$$

which deviates by 1.6σ from the CLEO result.

Taking these numbers at face value would be premature. We recall that we used both a chiral extrapolation (our computations were performed at $M_\pi = 470$ MeV and $M_\pi = 370$ MeV) and a model for the form factors $f_+^{D_s\to\eta}(q^2)$ and $f_+^{D_s\to\eta\prime}(q^2)$. Our result, however, demonstrates the potential that a future lattice study of the form factors $f_+^{D_s\to\eta}(q^2)$ and $f_+^{D_s\to\eta\prime}(q^2)$ will have. A study of these form factors, performed at the physical mass point, will significantly reduce the errors, which at present are dominated by systematics. We recall that the present work is mainly a pilot study to establish the feasibility of computations of form factors involving quark line disconnected diagrams.

V. CONCLUSIONS AND DISCUSSION

We calculated semileptonic decay form factors $f_0(q^2)$ for $D_s \to \eta\ell\bar{\nu}_\ell$ and $D_s \to \eta\prime\ell\bar{\nu}_\ell$ decays, by means of numerical lattice simulation. We included all disconnected fermion loop contributions. Despite the statistically noisy and computationally expensive disconnected part, we obtained the form factor at $q^2 = 0$ within statistical errors of less than 6%. The values at $q^2 = 0$ are $|f_0^{D_s\to\eta}| = 0.564(11)$ and $|f_0^{D_s\to\eta\prime}| = 0.437(18)$ at $M_\pi \approx 470$ MeV and $|f_0^{D_s\to\eta}| = 0.542(13)$ and $|f_0^{D_s\to\eta\prime}| = 0.404(25)$ at $M_\pi \approx 370$ MeV, where the errors are statistical only. The masses of the η and the $\eta\prime$ mesons are $M_\eta = M_\pi = 470.5(1.8)$ MeV and $M_{\eta\prime} = 1032(27)$ MeV at $M_\pi \approx 470$ MeV, and $M_\eta = 542.8(6.2)$ and $M_{\eta\prime} = 946(65)$ MeV at $M_\pi \approx 370$ MeV, keeping $2M_K^2 + M_\pi^2 \propto m_s + 2m_l$

approximately constant. The mixing angle in the octet-singlet basis for the $M_\pi \approx 370$ MeV case is $\theta_8 = -10.9(1.5)_{\text{stat}}(0.5)_{\text{fit}}^\circ$, $\theta_1 = -5.5(1.5)_{\text{stat}}(1.2)_{\text{fit}}^\circ$ and $\bar{\theta} = -7.7(0.9)_{\text{stat}}(0.8)_{\text{fit}}^\circ$ in the parametrization Eq. (29). There is no mixing in the flavor symmetric $M_\pi \approx 470$ MeV case. This means we have two different mixing angles, indicating higher Fock state contributions. We are not yet able to extrapolate the mixing angles, leading distribution amplitudes or masses to the physical point; however, assuming a monotonous dependence of the mixing angles on the light quark mass, their absolute values should increase toward the physical point.

It is interesting to note that the disconnected fermion loop contribution to $f_0^{D_s\to\eta\prime}$ is really significant. In Fig. 8 we saw that the relevant three-point function contains a large contribution from the disconnected diagram. This implies that the Okubo-Zweig-Iizuka (OZI) rule suppressed gluonic contribution is not suppressed in this decay mode due to the chiral anomaly, as is also indicated by the fact that singlet and octet $\eta\prime$ distribution amplitudes cannot be parametrized by a single angle, relative to the octet-singlet basis.

We calculated the scalar form factor $f_0(q^2)$ which does not require knowledge of the renormalization constants. In order to compare with experiment, however, the vector form factor $f_+(q^2)$ is more relevant, since, in the massless lepton limit, only $f_+(q^2)$ contributes to the decay width. Technically, a computation of $f_+(q^2)$ is of a similar level of complexity as the present study, and we plan to pursue this in the near future. Finally, we remark that this work is an exploratory study and the quark masses we used are not yet physical. Having verified that computations of disconnected contributions to form factors are feasible, lighter pion masses and larger volumes will be simulated, also extending the present study to decays with the ϕ in the final state.

APPENDIX A: DETAILS OF THE ESTIMATION OF DISCONNECTED LOOPS

In this appendix we explain the methods implemented to calculate the disconnected loop given in Eq. (3). For convenience we restate the equation as

$$C_{1\text{pt}}(t, \boldsymbol{p}; x_0) = \sum_{\boldsymbol{x}} \exp(i\boldsymbol{p} \cdot (\boldsymbol{x} - x_0)) C_{1\text{pt}}(t, \boldsymbol{x}), \quad (A1)$$

$$C_{1\text{pt}}(t, \boldsymbol{x}) = \text{tr}\left[\sum_{\boldsymbol{x}', \boldsymbol{x}'} \Gamma \phi(\boldsymbol{x}, \boldsymbol{x}'') M^{-1}(t, \boldsymbol{x}''; t, \boldsymbol{x}') \phi(\boldsymbol{x}', \boldsymbol{x})\right]. \quad (A2)$$

The all-to-all propagator, $M^{-1}(t, \boldsymbol{x}''; t, \boldsymbol{x}')$, is computed using low mode deflation combined with stochastic estimation. This involves calculating n_{low} (exact) low eigenmodes (in absolute magnitude) of the Hermitian Dirac operator $Q = \gamma_5 M$,

$$Q|\lambda_i\rangle = \lambda_i|\lambda_i\rangle, \quad (A3)$$

where the λ_i are real. The low mode contribution to M^{-1} is given by

$$M^{-1}|_{\text{low}} = \sum_i \frac{1}{\lambda_i}|\lambda_i\rangle\langle\lambda_i|\gamma_5. \quad (A4)$$

For small quark masses the low modes give the most singular directions of M^{-1} and the higher mode contributions $M^{-1}|_{\text{high}} = M^{-1} - M^{-1}|_{\text{low}}$ become small. These higher modes are estimated stochastically using $\frac{1}{\sqrt{2}}(\mathbb{Z}_2 + i\mathbb{Z}_2)$ noise vectors, which approximately span a complete set

$$\frac{1}{n_{\text{stoch}}} \sum_{s=1}^{n_{\text{stoch}}} |\eta_s\rangle\langle\eta_s| = 1 + O\left(\frac{1}{\sqrt{n_{\text{stoch}}}}\right). \quad (A5)$$

We have

$$M^{-1}|_{\text{high}} = \frac{1}{n_{\text{stoch}}} \sum_{s=1}^{n_{\text{stoch}}} M^{-1}|\tilde{\eta}_s\rangle\langle\eta_s|, \quad (A6)$$

where

$$|\tilde{\eta}_s\rangle = \gamma_5 \left(1 - \sum_{i=1}^{n_{\text{low}}} |\lambda_i\rangle\langle\lambda_i|\right) \gamma_5|\eta_s\rangle \quad (A7)$$

is the source vector projected onto the subspace of the higher modes.

Stochastic estimation introduces additional (possibly dominant) noise on top of the gauge noise, and this needs to be reduced. We implemented a number of techniques to achieve this:

(1) Time and spin partitioning [41]. The stochastic sources were given nonzero values only on every fourth time slice and for a single spin index. To reconstruct the full propagator at every time slice requires $4(\text{spin}) \times 4(\text{time}) = 16$ inversions.

(2) Hopping parameter acceleration (HPA) [42]. A Wilson-type Dirac operator

$$M = \frac{1}{2\kappa}(1 - \kappa D) \quad (A8)$$

satisfies the identity

$$M^{-1} = 2\kappa \sum_{i=0}^{\infty} (\kappa D)^i = 2\kappa \sum_{i=0}^{n-1} (\kappa D)^i + (\kappa D)^n M^{-1} \quad (A9)$$

for any integer $n \geq 0$. When this expression is inserted into Eq. (A2), the first n terms may be zero, where the value of n depends on Γ and the form of the Dirac operator. With stochastic estimation of M^{-1} these terms will only contribute to the noise and can be omitted, giving $(\kappa D)^n M^{-1}$ as an improved estimate of M^{-1}.

Combining this with low mode deflation we have

$$M^{-1} = \sum_{i=1}^{n_{\text{low}}} \frac{1}{\lambda_i} (\kappa D)^n |\lambda_i\rangle\langle\lambda_i|\gamma_5$$

$$+ \frac{1}{n_{\text{stoch}}} \sum_{s=1}^{n_{\text{stoch}}} (\kappa D)^n M^{-1}|\tilde{\eta}_s\rangle\langle\eta_s|. \quad (A10)$$

For the clover action and $\Gamma = \gamma_5$ we can use $n = 2$.

(3) The truncated solver method (TSM) [43]. This method involves truncating the solver after a few iterations. The (hopefully small) correction to this truncation is calculated using a smaller number of stochastic estimates,

TABLE VI.   Parameters for the estimation of the disconnected loop. If the TSM is used, n_{stoch} stands for $N_1 + N_2$, where N_1 and N_2 are the numbers of stochastic estimates used for the truncated part and to estimate the bias, respectively. Note that due to the use of spin and time dilution, each stochastic estimation requires 16 inversions of the noise vector.

Set	Quark	n_{low}	n_{stoch}	TSM
S	l, s	24	$10 + 3$	Truncated after 150 CG iterations
A	l	40	$24 + 8$	Truncated after 120 CG iterations
	s	40	48	(Without TSM)

$$\frac{1}{n_{\text{stoch}}} \sum_{s=1}^{n_{\text{stoch}}} M^{-1} |\tilde{\eta}_s\rangle\langle\eta_s| \mapsto \frac{1}{N_1} \sum_{s=1}^{N_1} M^{-1}_{\text{trunc}} |\tilde{\eta}_s\rangle\langle\eta_s|$$

$$+ \frac{1}{N_2} \sum_{s=N_1+1}^{N_1+N_2} (M^{-1} - M^{-1}_{\text{trunc}}) |\tilde{\eta}_s\rangle\langle\eta_s|, \qquad (A11)$$

where $N_2 < N_1$. The truncated part is calculated with a conjugate gradient (CG) solver, while for $M^{-1}|\tilde{\eta}_s\rangle$ we use the domain decomposition solver implementation of Ref. [40]. To obtain the full expression for M^{-1} using HPA and low mode deflation one substitutes Eq. (A11) into Eq. (A10).

The parameters for the various techniques are chosen so that the stochastic error is minimized for fixed computational cost; see Ref. [11] for details. Our optimal choices are listed in Table VI. We found the HPA to be the most cost efficient noise reduction technique for our problem. The TSM only provided a slight improvement, due to the use of smeared loops. In general, the advantage of using the TSM will also depend on the efficiency of the solver.

Finally, we note that due to parity and charge conjugation considerations the disconnected loop in position space, $C_{1\text{pt}}(t, \boldsymbol{x})$, is real for $\Gamma = \gamma_5$. This means the imaginary part of our stochastic estimation of $C_{1\text{pt}}(t, \boldsymbol{x})$ only contributes to the noise, and we can set it to zero.

APPENDIX B: TWO-POINT FUNCTIONS

In the octet-singlet basis, we need the following two-point functions:

$$\langle \mathcal{O}_8(t;\boldsymbol{p})\mathcal{O}_8^\dagger(0)\rangle = \frac{1}{3}\langle(C_{ll} + C_{ss} - 2D_{ll} - 2D_{ss} + 2D_{ls} + 2D_{sl})\rangle, \qquad (B1)$$

$$\langle \mathcal{O}_1(t;\boldsymbol{p})\mathcal{O}_1^\dagger(0)\rangle = \frac{1}{3}\langle(2C_{ll} + C_{ss} - 4D_{ll} - D_{ss} - 2D_{ls} - 2D_{sl})\rangle, \qquad (B2)$$

$$\langle \mathcal{O}_1(t;\boldsymbol{p})\mathcal{O}_8^\dagger(0)\rangle = \frac{\sqrt{2}}{3}\langle(C_{ll} - C_{ss} - 2D_{ll} + D_{ss} + 2D_{ls} - D_{sl})\rangle, \qquad (B3)$$

$$\langle \mathcal{O}_8(t;\boldsymbol{p})\mathcal{O}_1^\dagger(0)\rangle = \langle \mathcal{O}_1(t;\boldsymbol{p})\mathcal{O}_8^\dagger(0)\rangle^*, \qquad (B4)$$

where $C_{aa} = C_{aa}(t, \boldsymbol{p})$ is a connected two-point function of quark flavor $a = l, s$ and D_{ab} is the disconnected two-point function of quark flavors a and b,

$$D_{ab}(t, \boldsymbol{p}) = \frac{a^4}{V_4} \sum_{t_0/a=0}^{T/a-1} C_{1\text{pt}}^a(t + t_0, \boldsymbol{p}) C_{1\text{pt}}^b(t_0, -\boldsymbol{p}), \qquad (B5)$$

where T is the temporal lattice size, V_4 is the four-volume and $C_{1\text{pt}}^a(t, \boldsymbol{p})$ is the disconnected fermion loop, Eq. (3), for quark flavor a.

The calculation of $C_{1\text{pt}}^a(t, \boldsymbol{p})$ is detailed in Appendix A. For the connected two-point function, we implemented low mode averaging (LMA) [23,24] reusing the eigenmodes computed for the evaluation of the disconnected loop. As discussed in Ref. [44], LMA works very efficiently for pseudoscalar meson two-point functions. We used LMA for both the connected light-light (C_{ll}) and strange-strange (C_{ss}) two-point functions.

A connected two-point function with LMA is given by

$$C_{\text{LMA}}^{2\text{pt}}(t, \boldsymbol{p}) = C_{\text{pa}}^{2\text{pt}}(t, \boldsymbol{p}; x_0) - C_{\text{low,pa}}^{2\text{pt}}(t, \boldsymbol{p}; x_0) + C_{\text{low}}^{2\text{pt}}(t, \boldsymbol{p}), \qquad (B6)$$

where $C_{\text{pa}}^{2\text{pt}}(t, \boldsymbol{p}; x_0)$ is the standard point-to-all two-point function, calculated with a single source point at $x_0 = (t_0, \boldsymbol{x}_0)$. For simplicity, we have suppressed the quark flavor index and, initially, do not consider quark smearing. In Eq. (B6), the low mode contribution to the point-to-all two-point function,

$$C_{\text{low,pa}}^{2\text{pt}}(t, \boldsymbol{p}; x_0)$$

$$= \sum_{\boldsymbol{x}} \exp(i\boldsymbol{p} \cdot \boldsymbol{x}) \sum_{i,j=1}^{n_{\text{low}}} \frac{1}{\lambda_i \lambda_j} \langle \lambda_i(x_0)|\gamma_5 \Gamma^\dagger|\lambda_j(x_0)\rangle$$

$$\times \langle \lambda_j(x + x_0)|\gamma_5 \Gamma|\lambda_i(x + x_0)\rangle, \qquad (B7)$$

where $x = (t, \boldsymbol{x})$ and $\Gamma = \gamma_5$ at the source and sink, is subtracted and replaced by the low mode contribution averaged over all lattice points,

$$C_{\text{low}}^{\text{2pt}}(t, \boldsymbol{p}) = \frac{a^4}{V_4} \sum_{x_0} C_{\text{low,pa}}^{\text{2pt}}(t, \boldsymbol{p}; x_0). \tag{B8}$$

Smearing the quarks is implemented by replacing the eigenvectors $|\lambda_i\rangle$ in Eq. (B7) with smeared vectors, $\phi|\lambda_i\rangle$, for a smearing function ϕ.

Finally, we averaged over forward and backward propagating two-point functions, as well as rotationally equivalent momentum combinations.

APPENDIX C: THREE-POINT FUNCTIONS

The three-point function we need to determine is

$$\langle C_{\text{3pt}}^{D_s \to \eta^{(\prime)}}(t, \boldsymbol{p}, \boldsymbol{k}; t_{\text{sep}}, x_0) \rangle = \langle 0 | \mathcal{O}_{\eta^{(\prime)}}(\boldsymbol{k}, t_{\text{sep}} + t_0) S(\boldsymbol{q}, t + t_0) \mathcal{O}_{D_s}^\dagger(t_0, \boldsymbol{x}_0) | 0 \rangle$$
$$= \sum_{\boldsymbol{x}, \boldsymbol{y}} e^{i\boldsymbol{k}\cdot\boldsymbol{x}} e^{i\boldsymbol{q}\cdot\boldsymbol{y}} \langle 0 | \mathcal{O}_{\eta^{(\prime)}}(t_{\text{sep}} + t_0, \boldsymbol{x} + \boldsymbol{x}_0) S(t + t_0, \boldsymbol{y} + \boldsymbol{x}_0) \mathcal{O}_{D_s}^\dagger(t_0, \boldsymbol{x}_0) | 0 \rangle, \tag{C1}$$

where $\mathcal{O}_{\eta^{(\prime)}}$, $\mathcal{O}_{D_s}$ are the interpolators, S is the local scalar current and $\boldsymbol{p} = \boldsymbol{q} + \boldsymbol{k}$. The interpolators for η and η' are obtained from Eq. (7), by solving the generalized eigenvalue problem for each $\boldsymbol{k}$. For $\boldsymbol{k} = \boldsymbol{0}$, we used the improved mixing angles θ and θ' as discussed in Sec. III.

We need both connected and disconnected contributions to calculate the three-point function Eq. (C1); see Fig. 1. For the connected part, we used the stochastic method detailed in Ref. [45]. This approach allows us to access many momentum combinations at a lower computational cost compared to the standard sequential source method. We compute all rotationally equivalent momentum combinations and average over these.

The disconnected part is obtained from combining a connected charm-strange two-point function, $C_{\text{cs}}(t, \boldsymbol{q}; x_0)$, with a one-point quark loop of flavor a,

$$C_{\text{disc}}^{\text{3pt},a}(t, t_{\text{sep}}, \boldsymbol{p}, \boldsymbol{k}; x_0) = C_{\text{1pt}}^a(t_0 + t_{\text{sep}}, \boldsymbol{k}; x_0) C_{\text{cs}}(t, \boldsymbol{q}; x_0), \tag{C2}$$

and

$$C_{\text{cs}}(t, \boldsymbol{q}; x_0) = \sum_{\boldsymbol{x}} \exp(i\boldsymbol{q}\cdot\boldsymbol{x}) \text{tr}[M_c^{-1}(x + x_0; x_0)\gamma_5 M_s^{-1}(x_0; x + x_0)]. \tag{C3}$$

Note that the charm-strange two-point function has a pseudoscalar source and a scalar sink. The one-point loop is calculated as described in Appendix A.

We employ low mode averaging in a similar way to that used for the computation of the connected two-point function in Appendix B, by averaging the low mode contributions to $C_{\text{disc}}^{\text{3pt},a}$ over x_0:

$$C_{\text{disc,LMA}}^{\text{3pt},a}(t, t_{\text{sep}}, \boldsymbol{p}, \boldsymbol{k}; x_0) = C_{\text{1pt}}^a(t_0 + t_{\text{sep}}, \boldsymbol{k}; x_0)[C_{\text{cs}}(t, \boldsymbol{q}; x_0) - C_{\text{low,pa}}(t, \boldsymbol{q}; x_0)]$$
$$+ \frac{1}{N_y} \sum_{\boldsymbol{y}} C_{\text{1pt}}^a(t_0 + t_{\text{sep}} + t_y, \boldsymbol{k}; x_0 + y) C_{\text{low,pa}}(t, \boldsymbol{q}; x_0 + y)), \tag{C4}$$

where

$$C_{\text{low,pa}}(t, \boldsymbol{q}; x_0) \equiv \sum_{\boldsymbol{x}} \exp(i\boldsymbol{p}\cdot\boldsymbol{x}) \sum_{i=1}^{n_{\text{low}}} \frac{1}{\lambda_i} \text{tr}[M_c^{-1}(x + x_0; x_0)\gamma_5 |\lambda_i(x_0)\rangle \langle \lambda_i(x + x_0)|] \tag{C5}$$

and

$$C_{\text{1pt}}^a(t_0 + t_{\text{sep}} + t_y, \boldsymbol{k}; x_0 + y) = C_{\text{1pt}}^a(t_0 + t_{\text{sep}} + t_y, \boldsymbol{k}; x_0) \exp(-i\boldsymbol{k}\cdot\boldsymbol{y}). \tag{C6}$$
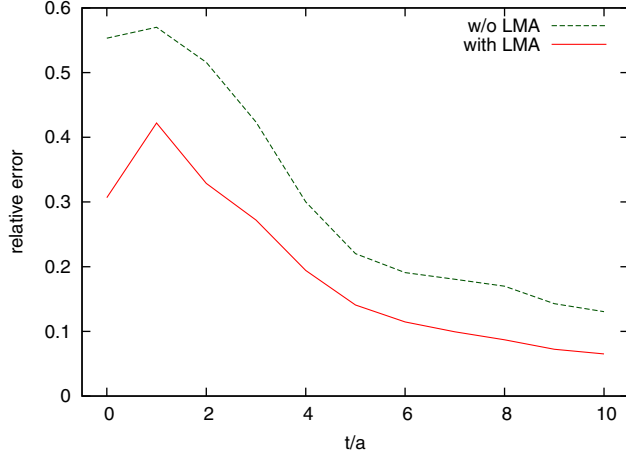
FIG. 12 (color online). The relative errors of the disconnected three-point function $\langle C_{\text{disc}}^{3\text{pt},l}(t, t_{\text{sep}}, \boldsymbol{p}, \boldsymbol{k}) \rangle$ with and without low mode averaging for Set S. The sink-source separation is $t_{\text{sep}} = 10a$, the D_s meson is located at $t = 0$ with lattice momentum $\boldsymbol{P} = (1,0,0)$ and the disconnected light-quark loop is located at $t/a = 10$ with momentum $\boldsymbol{K} = (1,0,0)$.

The eigenvalues, λ_i, and eigenvectors, $|\lambda_i\rangle$, are computed for the strange quark. We average over $N_y = 4^3 < V_4/a^4$ source points only, due to the computational cost of calculating the charm quark propagator, M_c^{-1}, for each source. We employ the subset $y = (t_y, \mathbf{y})$ with $t_y = 0$ and $\mathbf{y} = (n_1, n_2, n_3)L/(4a)$ with $n_i = 0, 1, 2, 3$.

Finally, we averaged over rotationally equivalent momentum combinations, and averaged over $+t_{\text{sep}}$ and $-t_{\text{sep}}$ for each value of sink-source separation $|t_{\text{sep}}|$. Figure 12 shows a typical example of a comparison of the relative error of the disconnected three-point function with and without low mode averaging. The figure illustrates that LMA reduces the error significantly.

APPENDIX D: DATA

The fitted values of two-point functions are listed in Tables VII and VIII. The values of the scalar form factor $f_0(q^2)$ at each q^2 are listed in Tables IX, X, XI and XII.

TABLE VII. The ground state energies E and energy gaps ΔE to the first excited state for zero and finite momenta for Set A. ΔE was obtained using Eq. (38). The mass of the η' meson is determined applying the improved method (see Sec. III). Also listed is the mass obtained by using the lattice dispersion relation Eq. (10) (lat. disp.).

	$\boldsymbol{p} \times L/(2\pi)$	Ground state			Excited state		
		Fit range	aE	χ^2/d.o.f.	Fit range	$a\Delta E$	χ^2/d.o.f.
π	(0,0,0)	12–24	0.141(01)	1.08	⋯	⋯	⋯
	(1,0,0)	9–17	0.296(03)	0.57	⋯	⋯	⋯
	(1,1,0)	8–17	0.409(18)	0.78	⋯	⋯	⋯
	(1,1,1)	6–11	0.522(82)	0.40	⋯	⋯	⋯
	(lat. disp.)[a]	⋯	0.141(01)	0.40	⋯	⋯	⋯
η	(0,0,0)	6–24	0.207(03)	0.73	2–4	0.638(91)	0.50
	(1,0,0)	9–23	0.328(05)	0.57	2–7	0.437(43)	0.16
	(1,1,0)	8–14	0.438(15)	0.71	2–4	0.645(219)	0.02
	(1,1,1)[b]	5–11	0.577(45)	0.26	⋯	⋯	⋯
	(lat. disp.)	⋯	0.206(02)	1.33	⋯	⋯	⋯
η'	(0,0,0)	7–11	0.309(38)	0.43	2–4	0.417(105)	0.03
	(1,0,0)	6–11	0.452(22)	0.06	2–4	0.815(716)	0.21
	(1,1,0)	6–10	0.552(40)	1.17	⋯	⋯	⋯
	(1,1,1)[b]	4–7	0.715(81)	0.30	⋯	⋯	⋯
	(lat. disp.)	⋯	0.360(25)	1.77	⋯	⋯	⋯
D_s	(0,0,0)	11–21	0.775(02)	0.15	2–6	0.356(98)	0.45
	(1,0,0)	11–21	0.814(03)	0.26	2–6	0.333(68)	0.47
	(1,1,0)	11–20	0.851(05)	0.58	2–6	0.324(62)	0.49
	(1,1,1)	11–21	0.886(07)	0.93	2–6	0.321(64)	0.52
	(2,0,0)	11–20	0.924(10)	0.18	2–6	0.371(116)	0.37
	(2,1,0)	11–20	0.959(15)	0.42	2–6	0.396(154)	0.39
	(lat. disp.)[a]	⋯	0.774(02)	0.41	⋯	⋯	⋯

[a]Not used.
[b]Not included in the dispersion relation.

TABLE VIII.   The same as Table VII for Set S.

	$\boldsymbol{p} \times L/(2\pi)$	Ground state			Excited state		
		Fit range	aE	χ^2/d.o.f.	Fit range	$a\Delta E$	χ^2/d.o.f.
η	(0,0,0)	14–24	0.179(01)	0.55	5–12	0.359(56)	0.79
$(=\pi)$	(1,0,0)	8–22	0.320(02)	1.37	2–5	0.574(34)	0.72
	(1,1,0)	8–18	0.420(05)	1.09	2–4	0.590(76)	0.15
	(1,1,1)	6–15	0.500(12)	0.64	2–5	0.648(101)	0.68
	(2,0,0)[b]	4–10	0.626(21)	0.22	$\cdots$	$\cdots$	$\cdots$
	(lat. disp.)[a]	$\cdots$	0.179(01)	5.44	$\cdots$	$\cdots$	$\cdots$
η'	(0,0,0)	4–11	0.417(23)	0.72	$\cdots$	$\cdots$	$\cdots$
	(1,0,0)	5–10	0.471(11)	0.98	$\cdots$	$\cdots$	$\cdots$
	(1,1,0)	6–12	0.511(17)	1.55	2–4	0.585(100)	0.56
	(1,1,1)	8–12	0.524(77)	0.66	$\cdots$	$\cdots$	$\cdots$
	(lat. disp.)	$\cdots$	0.392(10)	1.33	$\cdots$	$\cdots$	$\cdots$
D_s	(0,0,0)	11–24	0.769(01)	0.44	2–7	0.391(65)	0.60
	(1,0,0)	12–24	0.808(02)	0.37	2–7	0.365(56)	0.45
	(1,1,0)	12–24	0.846(03)	0.24	2–8	0.360(52)	0.27
	(1,1,1)	10–24	0.885(03)	0.32	2–8	0.399(38)	0.40
	(2,0,0)[b]	10–24	0.921(04)	0.24	2–6	0.407(47)	0.26
	(2,1,0)[b]	10–24	0.951(05)	0.28	2–6	0.379(39)	0.35
	(lat. disp.)[a]	$\cdots$	0.768(01)	0.48	$\cdots$	$\cdots$	$\cdots$

[a]Not used.
[b]Not included in the dispersion relation.

TABLE IX.   The $D_s \to \eta \ell \bar\nu_\ell$ scalar form factor $f_0(q^2)$ for Set A. The first column is a representative example for a given momentum combination. The last column (labeled "Equiv.") lists the number of equivalent momentum combinations. The fit ranges and $t_{\rm sep}$ used in the simultaneous fits are also listed. For the fit function, $R(t)$ in Eq. (40), "2 exp $+c$" indicates that all terms are included; i.e. c, A_1 and A_2 are free parameters of the fit.

$\boldsymbol{p}, \boldsymbol{q}, \boldsymbol{k} \times L/(2\pi)$	$a^2 q^2$	$f(q^2)$	$t_{\rm sep}/a$ [fit range]	Fit function	χ^2/d.o.f.	Equiv.
(0,0,0), (1,0,0), (−1,0,0)	0.129(05)	−0.615(19)	8[2–6], 10[2–8], 16[9–14]	2 exp $+c$	1.01	6
(1,0,0), (0,0,0), (1,0,0)	0.234(06)	−0.659(27)	8[2–6], 10[2–8], 16[9–14]	2 exp $+c$	0.85	6
(1,0,0), (1,1,0), (0,−1,0)	0.097(06)	−0.592(19)	8[2–6], 10[2–8], 16[9–14]	2 exp $+c$	0.71	24
(1,0,0), (2,0,0), (−1,0,0)	−0.040(06)	−0.544(18)	8[2–6], 10[2–8], 16[9–14]	2 exp $+c$	0.53	6
(1,1,0), (1,0,0), (0,1,0)	0.202(07)	−0.643(29)	8[2–6], 10[2–8], 16[10–14]	2 exp $+c$	0.72	24
(1,1,0), (1,1,1), (0,0,−1)	0.065(07)	−0.583(22)	8[2–6], 10[2–8], 16[9–14]	2 exp $+c$	0.65	24
(1,1,1), (1,1,0), (0,0,1)	0.172(10)	−0.607(30)	8[2–6], 10[2–8], 16[9–14]	2 exp $+c$	0.68	24
(0,0,0), (1,1,0), (−1,−1,0)	−0.023(10)	−0.515(21)	8[3–6], 10[3–8], 16[10–14]	2 exp $+c$	0.74	12
(1,0,0), (0,1,0), (1,−1,0)	0.073(11)	−0.539(27)	8[3–6], 10[3–8], 16[10–14]	2 exp $+c$	0.55	24
(1,0,0), (1,1,1), (0,−1,−1)	−0.064(11)	−0.481(24)	8[3–6], 10[3–8], 16[10–14]	2 exp $+c$	0.56	24
(1,1,0), (1,0,1), (0,1,−1)	0.034(12)	−0.526(30)	8[3–6], 10[3–8], 16[11–14]	2 exp $+c$	0.95	48
(1,1,0), (2,0,0), (−1,1,0)	−0.103(12)	−0.450(30)	8[3–6], 10[3–8], 16[11–14]	2 exp $+c$	0.82	24

TABLE X.   The $D_s \to \eta'\ell\bar{\nu}_\ell$ scalar form factor $f_0(q^2)$ for Set A, displayed as in Table IX. "1 exp +c" indicates that the parameter A_2 is set to zero in the fit.

$\boldsymbol{p},\boldsymbol{q},\boldsymbol{k} \times L/(2\pi)$	a^2q^2	$f(q^2)$	$t_{\rm sep}/a$ [fit range]	Fit function	$\chi^2/{\rm d.o.f.}$	Equiv.
(0,0,0), (1,0,0), (−1,0,0)	0.035(14)	0.394(44)	8[2–6], 10[4–8], 16[10–14]	2 exp +c	1.23	6
(1,0,0), (0,0,0), (1,0,0)	0.130(15)	0.395(76)	8[4–6], 10[4–8], 16[12–14]	2 exp +c	1.37	6
(1,0,0), (1,1,0), (0,−1,0)	−0.007(15)	0.357(50)	8[2–6], 10[4–8], 16[10–14]	2 exp +c	1.21	24
(1,0,0), (2,0,0), (−1,0,0)	−0.144(15)	0.356(39)	8[2–6], 10[4–8], 16[10–14]	2 exp +c	0.85	6
(1,1,0), (1,0,0), (0,1,0)	0.089(17)	0.491(80)	8[2–6], 10[4–8], 16[11–12]	2 exp +c	1.15	24
(1,1,0), (1,1,1), (0,0,−1)	−0.048(17)	0.350(56)	8[2–6], 10[4–8], 16[11–13]	2 exp +c	1.25	24
(0,0,0), (1,1,0), (−1,−1,0)	−0.088(17)	0.375(26)	8[3–5], 10[4–7], 16[10–13]	1 exp +c	0.50	12
(1,0,0), (0,1,0), (1,−1,0)	−0.000(20)	0.416(36)	8[3–5], 10[5–7], 16[10–13]	1 exp +c	0.46	24
(1,0,0), (1,1,1), (0,−1,−1)	−0.137(20)	0.360(29)	8[3–5], 10[4–7], 16[10–13]	1 exp +c	0.56	24
(1,1,0), (0,0,0), (1,1,0)	0.089(22)	0.510(59)	8[4–5], 10[4–7], 16[11–13]	1 exp +c	0.82	12
(1,1,0), (1,0,1), (0,1,−1)	−0.048(22)	0.441(42)	8[3–4], 10[4–7], 16[10–13]	1 exp +c	0.53	48
(1,1,0), (2,0,0), (−1,1,0)	−0.185(22)	0.353(33)	8[3–5], 10[4–7], 16[10–13]	1 exp +c	0.73	24
(1,1,1), (1,0,0), (0,1,1)	0.043(25)	0.481(71)	8[4–5], 10[4–7], 16[12–13]	1 exp +c	0.62	24
(2,0,0), (1,1,0), (1,−1,0)	0.001(29)	0.432(70)	8[4–5], 10[5–7], 16[11–13]	1 exp +c	0.88	24
(0,0,0), (1,1,1), (−1,−1,−1)	−0.201(12)	0.259(41)	8[4–5], 10[6–7], 16[11–13]	1 exp +c	1.21	8
(1,0,0), (0,1,1), (1,−1,−1)	−0.125(19)	0.266(56)	8[4–5], 10[6–7], 16[12–13]	1 exp +c	0.95	24
(1,1,0), (0,0,1), (1,1,−1)	−0.048(25)	0.336(93)	8[4–5], 10[6–7], 16[12–13]	1 exp +c	0.68	24

TABLE XI.   The $D_s \to \eta\ell\bar{\nu}_\ell$ scalar form factor $f_0(q^2)$ for Set S, displayed as in Table IX. Note that the $\chi^2/{\rm d.o.f.}$ refer to uncorrelated fits.

$\boldsymbol{p},\boldsymbol{q},\boldsymbol{k} \times L/(2\pi)$	a^2q^2	$f(q^2)$	$t_{\rm sep}/a$ [fit range]	Fit function	$\chi^2/{\rm d.o.f.}$	Equiv.
(0,0,0), (0,0,0), (0,0,0)	0.348(02)	−0.827(14)	16[7–10], 24[13–19]	2 exp +c	0.10	1
(1,0,0), (1,0,0), (0,0,0)	0.328(03)	−0.812(17)	16[7–10], 24[13–19]	2 exp +c	0.20	6
(1,1,0), (1,1,0), (0,0,0)	0.309(04)	−0.786(25)	16[8–11], 24[13–19]	2 exp +c	0.01	12
(1,1,1), (1,1,1), (0,0,0)	0.293(05)	−0.773(29)	16[8–10], 24[13–19]	2 exp +c	0.01	8
(0,0,0), (1,0,0), (−1,0,0)	0.133(02)	−0.610(16)	8[4–5], 10[4–7], 16[4–13], 24[13–19]	2 exp +c	0.51	6
(1,0,0), (0,0,0), (1,0,0)	0.239(02)	−0.658(25)	8[4–5], 10[4–7], 16[4–13], 24[12–19]	2 exp +c	0.20	6
(1,0,0), (1,1,0), (0,−1,0)	0.102(02)	−0.597(14)	8[4–5], 10[4–7], 16[4–13], 24[11–19]	2 exp +c	0.26	24
(1,0,0), (2,0,0), (−1,0,0)	−0.036(02)	−0.546(13)	8[4–5], 10[4–7], 16[4–13], 24[15–20]	2 exp +c	0.57	6
(1,1,0), (1,0,0), (0,1,0)	0.209(03)	−0.640(20)	8[4–5], 10[4–7], 16[4–13]	2 exp +c	0.35	24
(1,1,0), (1,1,1), (0,0,−1)	0.072(03)	−0.582(16)	8[4–5], 10[4–7], 16[4–13], 24[13–19]	2 exp +c	0.20	24
(0,0,0), (1,1,0), (−1,−1,0)	−0.015(03)	−0.550(23)	8[3–5], 10[3–7], 16[10–13], 24[18–21]	2 exp +c	0.07	12
(1,0,0), (0,1,0), (1,−1,0)	0.083(04)	−0.571(32)	8[3–5], 10[3–7], 16[8–13], 24[19–21]	2 exp +c	0.02	24
(1,0,0), (1,1,1), (0,−1,−1)	−0.054(04)	−0.513(22)	8[3–5], 10[3–7], 16[8–13], 24[17–21]	2 exp +c	0.31	24
(1,1,0), (1,0,1), (0,1,−1)	0.046(05)	−0.571(29)	8[3–5], 10[3–7], 16[8–13], 24[17–21]	2 exp +c	0.20	48
(1,1,0), (2,0,0), (−1,1,0)	−0.091(05)	−0.498(21)	8[2–6], 10[2–8], 16[2–14], 24[13–21]	2 exp +c	0.36	24
(0,0,0), (1,1,1), (−1,−1,−1)	−0.131(06)	−0.517(33)	8[2–6], 10[2–8], 16[10–14], 24[17–21]	2 exp +c	0.32	8
(1,0,0), (0,1,1), (1,−1,−1)	−0.039(07)	−0.504(36)	8[2–6], 10[2–8], 16[11–14]	2 exp +c	0.58	24

TABLE XII. The $D_s \to \eta' \ell \bar{\nu}_\ell$ scalar form factor $f_0(q^2)$ for Set S, displayed as in Table IX. "1 exp +c" indicates that the parameter A_2 is set to zero in the fit.

$\boldsymbol{p}, \boldsymbol{q}, \boldsymbol{k} \times L/(2\pi)$	$a^2 q^2$	$f(q^2)$	t_{sep}/a [fit range]	Fit function	χ^2/d.o.f.	Equiv.
(1,0,0), (1,0,0), (0,0,0)	0.086(15)	0.523(45)	8[2–6], 10[4–8], 16[12–14]	1 exp +c	1.12	6
(1,1,0), (1,1,0), (0,0,0)	0.049(16)	0.495(54)	8[2–6], 10[4–8], 16[12–14]	1 exp +c	1.00	12
(0,0,0), (1,0,0), (−1,0,0)	0.019(06)	0.430(24)	8[2–5], 10[3–7], 16[10–13]	1 exp +c	0.39	6
(1,0,0), (0,0,0), (1,0,0)	0.113(07)	0.464(35)	8[2–5], 10[3–7], 16[10–13]	1 exp +c	0.48	6
(1,0,0), (1,1,0), (0,−1,0)	−0.024(07)	0.417(27)	8[2–5], 10[3–7], 16[9–13]	1 exp +c	0.25	24
(1,0,0), (2,0,0), (−1,0,0)	−0.161(07)	0.371(27)	8[2–5], 10[3–7], 16[9–13]	1 exp +c	0.50	6
(1,1,0), (1,0,0), (0,1,0)	0.071(07)	0.451(42)	8[2–5], 10[3–7], 16[11–13]	1 exp +c	0.52	24
(1,1,0), (1,1,1), (0,0,−1)	−0.066(07)	0.415(33)	8[2–5], 10[3–7], 16[10–13]	1 exp +c	0.26	24
(1,1,1), (1,1,0), (0,0,1)	0.033(08)	0.468(44)	8[2–5], 10[3–7], 16[12–13]	1 exp +c	0.38	24
(0,0,0), (1,1,0), (−1,−1,0)	−0.069(08)	0.403(32)	8[2–6], 10[4–8], 16[9–14]	2 exp +c	0.98	12
(1,0,0), (0,1,0), (1,−1,0)	0.022(10)	0.427(45)	8[2–6], 10[4–8], 16[10–14]	2 exp +c	0.52	24
(1,0,0), (1,1,1), (0,−1,−1)	−0.115(10)	0.355(37)	8[2–6], 10[4–8], 16[11–14]	2 exp +c	0.58	24
(1,1,0), (1,0,1), (0,1,−1)	−0.022(11)	0.400(54)	8[2–6], 10[4–8], 16[11–14]	2 exp +c	0.36	48
(1,1,0), (2,0,0), (−1,1,0)	−0.159(11)	0.373(45)	8[2–6], 10[4–8], 16[10–14]	2 exp +c	0.54	24
(0,0,0), (1,1,1), (−1,−1,−1)	−0.147(33)	0.369(34)	8[2–5], 10[5–7], 16[10–13]	1 exp +c	0.82	8
(1,0,0), (0,1,1), (1,−1,−1)	−0.058(39)	0.342(45)	8[3–5], 10[5–7], 16[10–13]	1 exp +c	0.87	24

[1] G. Donald, C. Davies, J. Koponen, and G. Lepage (HPQCD Collaboration), Phys. Rev. D **90**, 074506 (2014).
[2] P. Colangelo and F. De Fazio, Phys. Lett. B **520**, 78 (2001).
[3] K. Azizi, R. Khosravi, and F. Falahati, J. Phys. G **38**, 095001 (2011).
[4] N. Offen, F. Porkert, and A. Schäfer, Phys. Rev. D **88**, 034023 (2013).
[5] C. Di Donato, G. Ricciardi, and I. Bigi, Phys. Rev. D **85**, 013016 (2012).
[6] J. Yelton *et al.* (CLEO Collaboration), Phys. Rev. D **80**, 052007 (2009).
[7] I. Kanamori, Proc. Sci., Confinement X (2012) 143.
[8] S. Collins, I. Kanamori, and J. Najjar, in Proceedings of the 6th International Workshop on Charm Physics (CHARM 2013), Manchester, 2013 edited by M. Gersabeck and C. Parkes.
[9] S. Collins, I. Kanamori, and J. Najjar, Proc. Sci., LAT-TICE2013 (2014) 392.
[10] H. Na, C. T. Davies, E. Follana, G. P. Lepage, and J. Shigemitsu, Phys. Rev. D **82**, 114506 (2010).
[11] G. Bali *et al.* (QCDSF Collaboration), Proc. Sci., LAT-TICE2011 (2011) 283.
[12] W. Bietenholz *et al.*, Phys. Lett. B **690**, 436 (2010).
[13] W. Bietenholz *et al.*, Phys. Rev. D **84**, 054509 (2011).
[14] N. Cundy *et al.*, Phys. Rev. D **79**, 094507 (2009).
[15] S. Sint and P. Weisz, Nucl. Phys. B, Proc. Suppl. **63**, 856 (1998).
[16] T. Bhattacharya, R. Gupta, W. Lee, S. R. Sharpe, and J. M. Wu, Phys. Rev. D **73**, 034504 (2006).
[17] S. Borsanyi *et al.*, J. High Energy Phys. 09 (2012) 010.
[18] R. Horsley, J. Najjar, Y. Nakamura, H. Perlt, D. Pleiter, P. E. L. Rakow, G. Schierrholz, A. Schiller, H. Stüben, and J. M. Zanotti, Proc. Sci., LATTICE2013 (2013) 249.
[19] G. Bali *et al.*, Proc. Sci., LATTICE2011 (2011) 135.
[20] S. Güsken, U. Löw, K.-H. Mütter, R. Sommer, A. Patel, and K. Schilling, Phys. Lett. B **227**, 266 (1989).
[21] S. Güsken, Nucl. Phys. B, Proc. Suppl. **17**, 361 (1990).
[22] M. Falcioni, M. Paciello, G. Parisi, and B. Taglienti, Nucl. Phys. **B251**, 624 (1985).
[23] T. A. DeGrand and S. Schäfer, Comput. Phys. Commun. **159**, 185 (2004).
[24] L. Giusti, P. Hernandez, M. Laine, P. Weisz, and H. Wittig, J. High Energy Phys. 04 (2004) 013.
[25] N. Christ, C. Dawson, T. Izubuchi, C. Jung, Q. Liu, R. D. Mawhinney, C. T. Sachrajda, A. Soni, and R. Zhou, Phys. Rev. Lett. **105**, 241601 (2010).
[26] E. B. Gregory, A. C. Irving, C. M. Richards, and C. McNeile (UKQCD Collaboration), Phys. Rev. D **86**, 014504 (2012).
[27] J. J. Dudek, R. G. Edwards, B. Joo, M. J. Peardon, D. G. Richards, and C. E. Thomas, Phys. Rev. D **83**, 111502 (2011).
[28] C. Michael, K. Ottnad, and C. Urbach, Phys. Rev. Lett. **111**, 181602 (2013).
[29] K. Olive *et al.* (Particle Data Group), Chin. Phys. C **38**, 090001 (2014).

[30] S. Aoki, H. Fukaya, S. Hashimoto, and T. Onogi, Phys. Rev. D **76**, 054508 (2007).

[31] S. O. Bilson-Thompson, D. B. Leinweber, and A. G. Williams, Ann. Phys. (Berlin) **304**, 1 (2003).

[32] C. Morningstar and M. J. Peardon, Phys. Rev. D **69**, 054501 (2004).

[33] G. S. Bali, N. Eicker, T. Lippert, H. Neff, B. Orth, K. Schilling, T. Struckmann, and J. Viehoff, Phys. Rev. D **64**, 054502 (2001).

[34] R. Brower, S. Chandrasekharan, J. W. Negele, and U. Wiese, Phys. Lett. B **560**, 64 (2003).

[35] T. Kaneko *et al.* (TWQCD Collaboration, JLQCD Collaboration), *Proc. Sci.*, LAT2009 (2009) 107.

[36] T. Feldmann, Int. J. Mod. Phys. A **15**, 159 (2000).

[37] D. Becirević and A. B. Kaidalov, Phys. Lett. B **478**, 417 (2000).

[38] P. Ball and R. Zwicky, Phys. Rev. D **71**, 014015 (2005).

[39] R. G. Edwards and B. Joó (SciDAC Collaboration, LHPC Collaboration, UKQCD Collaboration), Nucl. Phys. B, Proc. Suppl. **140**, 832 (2005).

[40] http://luscher.web.cern.ch/luscher/openQCD/index.html.

[41] S. Bernardson, P. McCarty, and C. Thron, Comput. Phys. Commun. **78**, 256 (1994).

[42] C. Thron, S. Dong, K. Liu, and H. Ying, Phys. Rev. D **57**, 1642 (1998).

[43] G. S. Bali, S. Collins, and A. Schäfer, Comput. Phys. Commun. **181**, 1570 (2010).

[44] G. Bali, L. Castagnini, and S. Collins, *Proc. Sci.*, LATTICE2010 (2010) 096.

[45] R. Evans, G. Bali, and S. Collins, Phys. Rev. D **82**, 094501 (2010).